DEVELOPMENT AND CHARACTERIZATION OF A LOW POWER HELIUM MICROWAVE INDUCED PLASMA FOR SPECTROMETRIC DETERMINATIONS OF METALS AND NONMETALS

by

Larry Donell Perkins

Dissertation submitted to the Faculty of the Virginia Polytechnic Institute and State University in partial fulfillment of the requirement for the degree of

Doctor of Philosophy

in

Chemistry

APPROVED:

Gary W. Long, Chairman

John G. Mason

Harold M. McNair

Larry T. Taylor

Roe-Hoan Yoon

DEVELOPMENT AND CHARACTERIZATION OF A LOW POWER HELIUM MICROWAVE INDUCED PLASMA FOR SPECTROMETRIC DETERMINATIONS OF METALS AND NONMETALS

by

Larry Donell Perkins

Gary L. Long, Chairman

Chemistry

(Abstract)

This dissertation centers on the development of a new helium microwave induced plasma. The analytical utility of this new plasma source is critically evaluated.

To sustain the helium plasma a TM_{010} high efficiency microwave induced plasma, HEMIP, was used. The HEMIP is a modification of the original Beenakker cavity that precludes the use of external matching devices, such as the highly popular double tuning stub.

The He-HEMIP was analytically characterized as an atomization source for metals and nonmetals with the use of atomic emission spectrometry (AES) and atomic fluorescence spectrometry (AFS). A torodial plasma was sustained in the cavity solely by the helium gas output of the nebulizer. Aqueous samples from a pneumatic glass nebulizer/Scott spray chamber were aspirated into the cavity without a desolvation

apparatus. With AES, detection limits for metals and nonmetals were in the sub-ppm range. With AFS, detection limits for metals were determined to be in the low ppm to sub-ppb range and were found to be not statistically different from those reported for HCL-ICP-AFS. Linear ranges for AES and AFS ranged from four up to five and one-half orders of concentrative magnitude. The effect of sample uptake rate on the emission intensity was investigated. Ionization interferences were determined to be minimal and phosphate interferences were found not to occur.

Development and characterization also included studies of the He-HEMIP's physical characteristics. Excitation and ionization temperatures were found to be approximately equal, suggesting that the He-HEMIP approaches local thermodynamic equilibrium.

Evaluation of the He-HEMIP as a routine detector for sulfur during coal pyrolysis and coal extracted samples was investigated. Results showed that the He-HEMIP is selective and sensitive. Detection values compared favorably to those of certified coal samples.

DEDICATION

This dissertation is dedicated to:

and to the memory of

(/ /10 - / /83)

ACKNOWLEDGEMENTS

To , my mother, I wish to express my thanks for your love, patience, and support during my educational endeavors.

I sincerely wish to thank Dr. Gary L. Long for his guidance and financial support during my graduate career at Virginia Polytechnic Institute and State University. Without your belief in me this dissertation would not be possible.

To the Plasmen (, , and), thanks for conversations that provided scientific assistance and friendship. a special thanks goes to you. always made time to listen and help. This indeed is a special quality. , your expertise in instrumental trouble shooting was indeed valuable.

To Drs. Taylor, McNair, Mason, and Yoon, thank you for your time and scientific assistance during my stay at VPI & SU. Special thanks goes to Andre Mollick for his talented glass blowing skills.

To , thank you for your friendship and encouragement. You assisted me in a time when few aided. Your attention and help will always be appreciated.

I would like to recognize the people whose friendships I have developed over the years;

, , ,

, , , ,

, , and . , thank you for your time spent editing this dissertation.

, you have shown me what an ideal friendship should be. Many thanks. I hope that our friendship can last for a lifetime.

TABLE OF CONTENTS

page

DEDICATION iii

ACKNOWLEDGEMENTS iv

LIST OF FIGURES vii

LIST OF TABLES ix

CHAPTER 1 INTRODUCTION 1

CHAPTER 2 EXPERIMENTAL CONSIDERATIONS 7

Reagents 7
Optical System 7
Sample Introduction 11
Microwave Cavity 15
Microwave Torch 19
Plasma Ignition and Operation 21
Plasma Behavior and Features 23
Limits of Detection 23
Data Presentation 24

CHAPTER 3 PHYSICAL MEASUREMENTS OF THE HELIUM HIGH EFFICIENCY MICROWAVE INDUCED PLASMA 25

EXPERIMENTAL 29

RESULTS AND DISCUSSION 37
Excitation Temperature 37
Ionization Temperature 40
Electron Number Density 42

CONCLUSIONS 44

CHAPTER 4 DETERMINATION OF AQUEOUS METALS BY MIP-AES AND MIP-AFS 47

EXPERIMENTAL 50

RESULTS AND DISCUSSION 50
Effect of Sample Uptake Rate 50
Organic Nebulization 52
Profiles 52
Linearity 54
Limits of Detection 54
Interelement Effects 56

CONCLUSIONS..... 62

CHAPTER 5 DETERMINATION OF NONMETALS BY MIP-AES..... 63

EXPERIMENTAL..... 67

RESULTS AND DISCUSSION..... 67
Wavelength Calibration..... 67
Carbon Observed Transitions..... 70
Fluorine Observed Transitions..... 70
Chlorine, Bromine, Phosphorus, and Iodine Observed Transitions..... 76
Sulfur Observed Transitions..... 79
Determination of Aqueous Nonmetals by Direct Nebulization..... 79
Determination of Nonmetals in NBS Simulated Rain Water..... 81

CONCLUSIONS..... 81

CHAPTER 6 DETERMINATION OF SULFUR IN COALS BY MIP-AES..... 85

EXPERIMENTAL..... 93

RESULTS AND DISCUSSION..... 98
Effect of the Chemical Composition of Coal: Matix Effects..... 98
Linearity..... 98
Sulfur Measurements..... 101

CONCLUSIONS..... 105

CHAPTER 7 CONCLUSIONS..... 106

REFERENCES..... 110

APPENDEX..... 115

VITA..... 121

LIST OF FIGURES

Figure		page
Figure 1:	Schematic diagram of atom-formation and processes	3
Figure 2:	Block diagram of the MIP-AES system	8
Figure 3:	Block diagram of the MIP-AFS system	9
Figure 4:	Viewing geometries used for He-HEMIP	12
Figure 5:	Purge system for the He-HEMIP	13
Figure 6:	Concentric nebulizer, spray chamber, and torch apparatus for He-HEMIP	14
Figure 7:	Diagram of the desolvation system	16
Figure 8:	Schematic diagram of the He-HEMIP	17
Figure 9:	Schematic of the tangential flow torch for the He-HEMIP	20
Figure 10:	Spatially intergrated electron number density profile, with (+) and without (Δ) water	43
Figure 11:	Spatial iodine intensity profile of position vs. intensity	45
Figure 12:	Effect of the sample uptake rate on the calcium emission intensity	51
Figure 13:	Radial emission profile for a 50 ppm calcium solution. Zero millimeter represents flush with the top of the cavity	53
Figure 14:	Effect of Na on the emission signal of a 10 ppm calcium solution	58
Figure 15:	Effect of Na on the fluorescence signal of a 10 ppm calcium solution	59
Figure 16:	Effect of phosphate on the calcium emission signal (calcium concentration = 10 ppm)	60
Figure 17:	Effect of phosphate on the calcium fluorescence signal (calcium concentration = 10 ppm)	61

Figure 18: Wavelength calibration device used for MIP-AES of nonmetals..... 68

Figure 19: Wavelength scans for carbon emission in the He-HEMIP..... 72

Figure 20: Partial Grotrian diagram of doublet atomic fluorine transitions..... 74

Figure 21: Partial Grotrian diagram of quartet atomic fluorine transitions..... 75

Figure 22: Addreviated wavelength scan for chlorine emission in the He-HEMIP..... 78

Figure 23: Reaction of sulfur compounds in coal pyrolysis chamber..... 88

Figure 24: Flow diagram for the determination of soluble sulfate in coal..... 95

Figure 25: Flow diagram for the determination of total sulfur by high temperature tube furnance combustion method (off-line)..... 96

Figure 26: Flow diagram for the determination of total sulfur by high temperature tube furnance combustion method (on-line)..... 97

Figure 27: Sulfur calibration curve..... 99

Figure 28: Plot of percent sulfur vs. time in the pyrolysis chamber using the on-line method. 104

LIST OF TABLES

Table		page
Table 1:	Equipment used in MIP-AES and MIP-AFS.....	10
Table 2:	Operational parameters.....	22
Table 3:	Wavelengths and constants used for iron temperature determinations.....	31
Table 4:	Wavelengths and constants used for helium temperature determinations.....	32
Table 5:	Data for Saha-Eggart electron number density determinations.....	38
Table 6:	Excitation temperatures by slope method.....	39
Table 7:	Excitation temperatures for several helium MIPs.....	41
Table 8:	MIP-AES metal detection limits in ppb (k=2).	55
Table 9:	MIP-AFS metal detection limits in ppb (k=2).	57
Table 10:	Organic solvents usd for nonmetal emission measurements.....	69
Table 11:	Carbon Lines observed in the He-HEMIP.....	71
Table 12:	Most intense Fluorine Emission Lines Observed in the He-HEMIP.....	73
Table 13:	Most intense Cl, P, I, and Br lines observed in the He-HEMIP.....	77
Table 14:	Sulfur emission lines observed in the He-HEMIP.....	80
Table 15:	He-HEMIP nonmetal detection limits in ppm (k=2).....	82
Table 16:	Values for the determination of nonmetals in NBS 2694 Simulated Rain Water.....	83
Table 17:	Emission signals at 180.7 nm using various standards (1000 ppm) for sulfur.....	100
Table 18:	Values for the determination of soluble	

sulfur in coals..... 102

Table 19: Values for the determination of total sulfur using the off-line method..... 103

Chapter 1

Introduction

The ideal atomic spectrometric source should excite emission from any element in the periodic table, be highly sensitive and stable, posess freedom from both spectral and chemical interferences, accept gaseous, liquid, or solid samples, and be inexpensive and easy to operate. Plasma sources, such as the popular inductively coupled plasma (ICP), fulfill many of these requirements thus being superior to arc/spark and flame methods of trace analysis [1-6]. When argon is used as the support gas, these inert gas discharges are characterized by a high temperture resulting in the sensitive determination of a large number of elements. Within the last 20 years, the microwave induced plasma (MIP) has evolved as a powerful excitation source, enabling plasmas to be sustained in argon, helium, nitrogen and, air [7-9].

The microwave induced plasma (MIP) is essentially a plasma discharge of either helium, argon, nitrogen, or air. It is maintained by a plasma supporting structure (resonance cavity) which is a hollow metal container that allows a standing electromagnetic wave to be established within it, or along it. Since the standing wave is at microwave

frequencies (usually 2450 MHz), the cavity size is on the order of several centimeters [8].

To generate the standing wave, microwave energy is sent into the cavity by means of a circuit loop, circuit short, or antenna which is connected to a microwave power supply via a coaxial cable or waveguide. The plasma gas is then passed through the cavity and ionized, with its energy coupled to the gaseous ions to produce the discharge. Transverse electric and magnetic waves enable such a configuration to exist [8].

Historically, sample introduction into the MIP has been limited to gaseous samples by gas chromatography or gaseous introduction via chemical hydration [7]. Research in the area of introducing aqueous sample directly into the MIP has been limited. The reason for is that the typical Beenakker cavity is not capable of completing the atomization cycle (Figure 1). The atomization cycle includes nebulization, desolvation, vaporization, atomization and excitation of the analyte. In order to complete this cycle, thus promoting excitation, the MIP must posess a high energy density and a sufficient kinetic temperature to promote the above processes; this does not occur with classical Beenakker cavities. Therefore, in order for the MIP to take its place in the area of atomic spectrometry, problems associated with the introduction of liquid samples must be overcome.

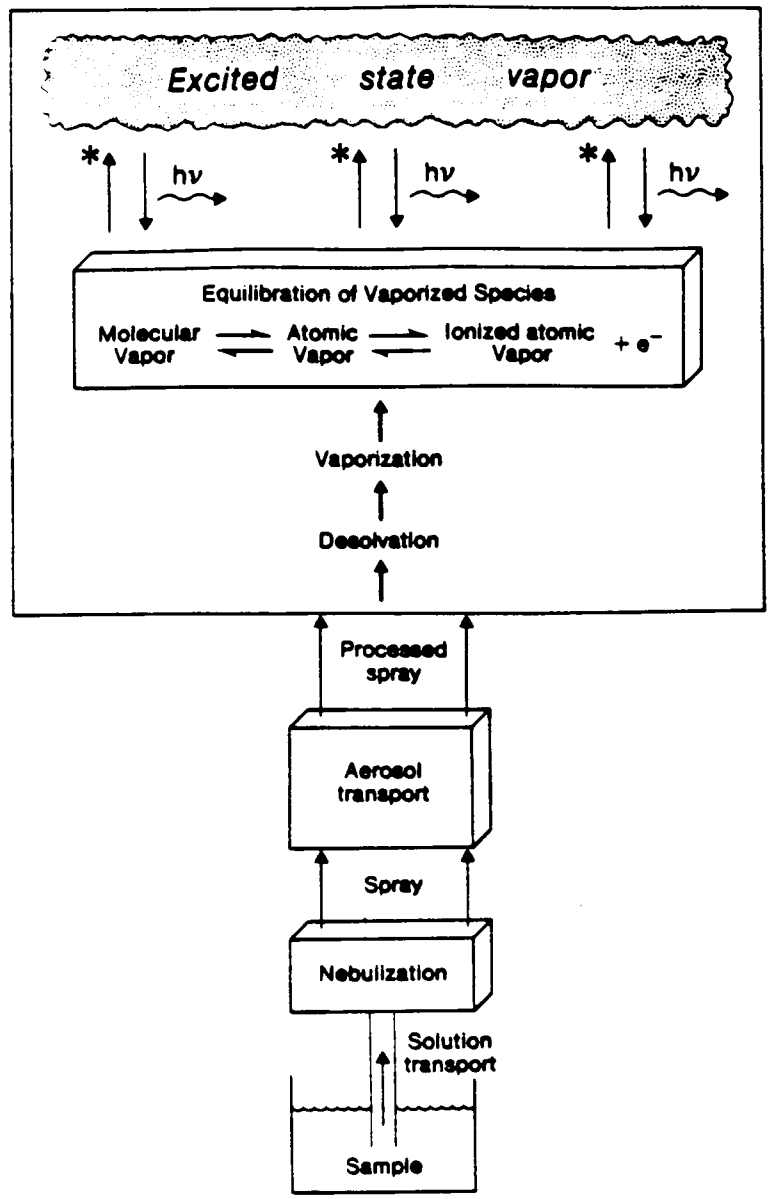

FIGURE 1: Schematic diagram of atom-formation processes (From Ref. 48).

One of the most attractive aspects of liquid sample introduction is its relative simplicity and reliability: coupled with the fact that a sample dissolution step is often necessary to produce suitable sampling statistics [10-11].

Direct sample introduction into the MIP thus represents a renaissance in MIP-AES technology. Literature on the direct introduction of aqueous sample introduction into the MIP has been separated into two areas by researchers: high power and low power [12]. High power microwave induced plasmas are those maintained above 150 W. Several reviews have appeared on the use of the MIP for atomic spectrometry and have included sample introduction techniques [7-9].

Beenakker et al. [13] introduced aqueous metal samples into the Ar plasma without desolvation at a sample uptake rate of 1.7 mL/min. A 150 W plasma was used to sustain the plasma. Satisfactory AES performance was obtained, but the use of the wet aerosol decreased the sensitivity by a factor of between 2 and 10, depending on the element studied.

Hass and Caruso was successful in introducing 0.81 mL/min of aqueous solution into a 500 W plasma for the study of metal ions in synthetic ocean water using a total Ar flow of 450 mL/min. Nebulizers included both concentric and frit. Detection limits were comparable to the ICP. The authors

reported severe microwave leakage using their 500 W argon plasma [14].

In a similar study, Ng and Shen [15] used a 105-115 W Ar plasma to introduce synthetic ocean water at a MAK nebulization uptake rate of 1.4 mL/min. The total Ar flow used in the study was reported at 537 mL/min. Detection limits compared favorably with the work of Beenakker.

In all but one report, reviewed references used argon as the plasma gas for direct nebulization of aqueous metals. The reason is that an argon plasma is easy to ignite and to sustain when compared to helium using the typical Beenakker cavity (helium has a greater electrical resistivity, heat capacity and thermal conductivity). However, Beenakker was able to sustain a helium plasma while introducing aqueous samples by using a low-flow nebulizer [16]. Unfortantly, the presence of larger droplets degraded signal stability.

The ability to sustain a helium plasma while introducing aqueous samples is of great importance for the following reasons: (1) the background continuum in the He plasma are about an order of magnitude weaker than that of Ar [17]; (2) He has greater optical transparancy at shorter wavelengths than Ar [17]; (3) the high excitation energies of a He plasma enables the production of analyte emission from states having energies in excess of 16 eV [18]. Simply stated, He has a higher excitation energy than Ar, which

will allow for the detection of every element on the perdioc table. In addition, their are fewer He lines to produce potentional spectral interferences.

The purpose of this work were: (1) to develop a new MIP system based on He as the support gas using a high efficiency cavity; (2) to investigate direct aqueous sample introduction as a viable alternative to conventional sample introduction (gaseous) for MIP-AES; (3) to conduct fundamental physical studies of the helium plasma; (4) to develop a method which can be applied routinely and universally to the determination of aqueous metals and nonmetals bases on atomic emission spectrometry and atomic fluoresence spectrometry; (5) to develop a sensitive and selective detector for sulfur during coal pyrolysis.

CHAPTER 2

EXPERIMENTAL CONSIDERATIONS

Reagents

All chemicals used were analytical reagent grade. Water was distilled and deionized. Stock solutions of all aqueous metals were purchased as 1000 ppm (Buck Scientific, Inc.) or prepared following standard procedures [19]. Iron for organic solvent determinations, was prepared by dissolving ferrocene in xylenes to obtain a 1000 ppm solution. Volumetric dilutions of these solutions were performed to obtain desired concentrations.

Coal samples were prepared by sieving the powered coal through a 200 mesh (75 micron) screen to remove large particles and aggregations, and weighing the fine powder in a sulfur and carbon free ceramic boat (Fisher Scientific).

The plasma gas used was Airco analytical-grade helium.

Optical System

The atomic emission and atomic fluorescence systems used in this work are shown in Figures 2 and 3, respectively. Table 1 lists all optical, electrical, and gas handling equipment, along with their manufacturers.

Emission from the plasma was focused onto the entrance slit of the monochromator (0.25 m monochromator for AFS and

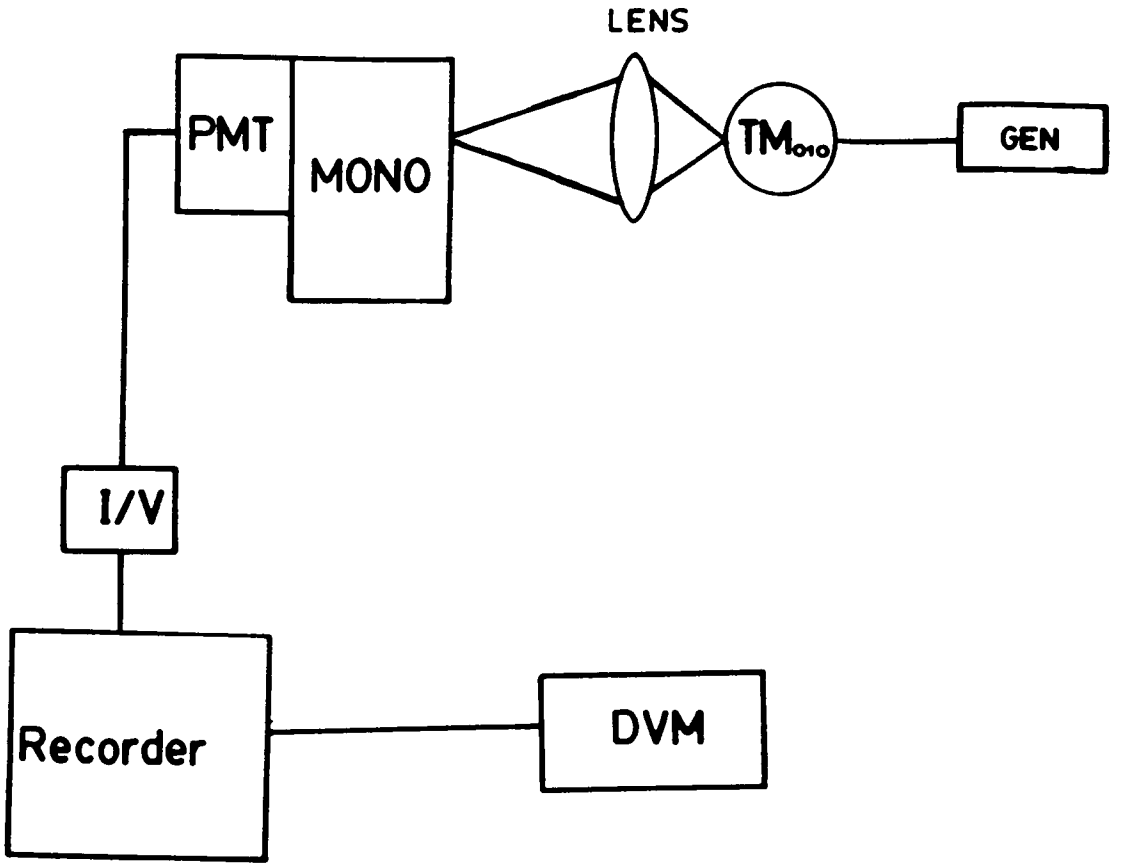

FIGURE 2: Block diagram of the MIP-AES system.

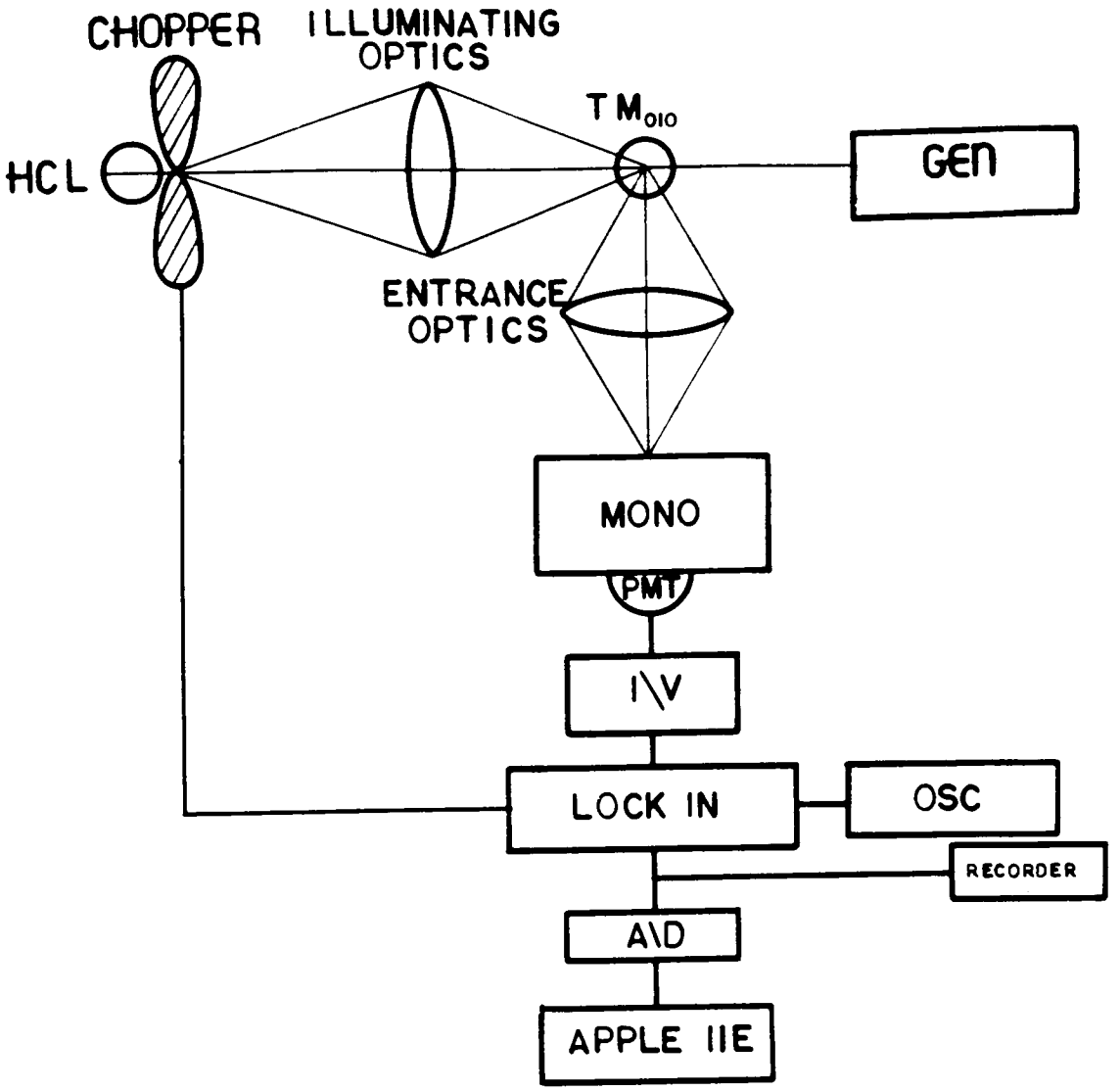

FIGURE 3: Block diagram of the MIP-AFS system.

TABLE 1: Equipment used in MIP-AES and MIP-AFS

Component	Model/Size	Manufacturer
Microwave Cavity	High-efficiency TM_{010}	Laboratory built
Generator	HI-2450	Holaday Industries Edinia, MN
Discharge Tube	Tangential	Laboratory built
Coaxial Cable	RG 214	Times Fiber Co. Wallingford, CT
Monochromator	01-512 0.25 m	PTI Princeton, NJ
PMT	R955	Hamamatsdu Corp Bridgewater, NJ
Nebulizer	concentric TR-50-C2	J. C. Meinhard Santa Anna, CA
Spray Chamber Constructed	Scott	Laboratory
Chopper	Model 125A	EG & G Princeton, NJ
Lock-in	Model 5101	EG & G Princeton, NJ
Lens	f/3, suprasil	Oriel Corp Stratford, CT
Computer	Apple IIe	Apple Computer Inc. Cupertino, CA
Flow Controllers	MM3	Air Products Allentown, PA

AES of metals; 0.35 m monochromator for nonmetal determinations) using a f/3 lens for one to one imagining. Current signals from the photomultiplier tube were converted to voltage using a current to voltage converter, in order to make the final signal compatible with the input of the analog-to-digital converter (ADALAB, Pittsburg, PA) on the Apple IIe computer.

Two different viewing geometries were used for collection of data with the He-HEMIP, Figure 4. Studies of metal atomic emission and atomic fluorescence were conducted with the plasma in the radial position (side-on), unless otherwise stated. An axial observation position (end-on) was used for all nonmetal studies.

In order to use the emission lines below 190 nm, the monochromator and optical path must be evacuated and purged with an inert gas. The laboratory constructed purge system is shown in Figure 5. The purge system consists of pyrex glass and rubber o-rings connected to an aluminum plate which is attached to the entrance slits of the monochromator. Argon was used as the purge gas.

Sample Introduction

Sample solutions were introduced into the plasma with a typical ICP-AES pneumatic nebulizer/Scott spray chamber system. A diagram of the sample introduction system is shown in Figure 6. The nebulizer, while operated at a flow

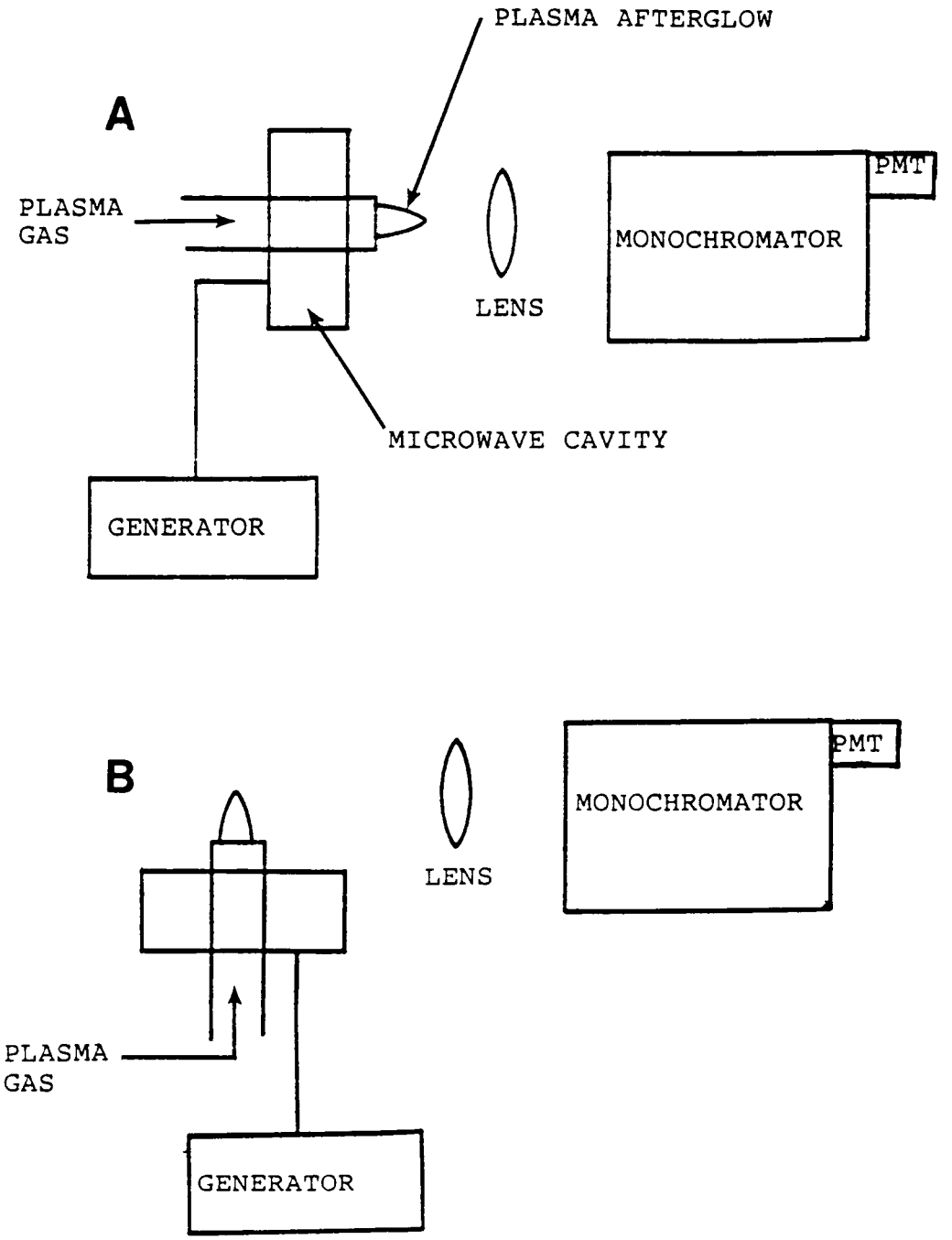

FIGURE 4: Viewing geometries used for the He-HEMIP. A represents the axial position and B the radial position.

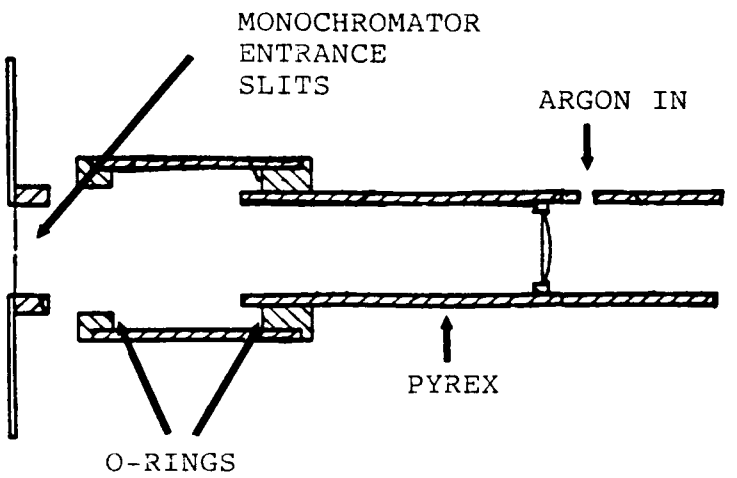

FIGURE 5: Purge system for the He-HEMIP.

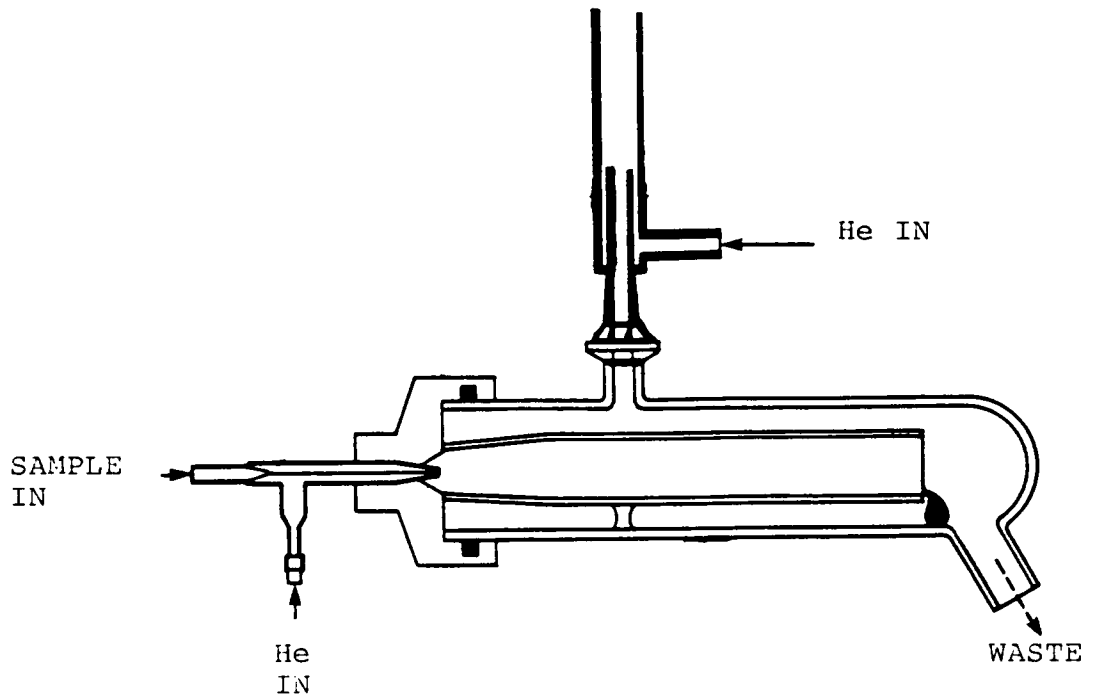

FIGURE 6: Concentric nebulizer, Scott spray chamber, and torch apparatus for the He-HEMIP.

rate of 1 L/min of He gas aspirated sample solution at a rate of 0.46 mL/min. The resulting aerosol passed through the spray chamber en-route to the He-HEMIP. All liquid sample introduction was conducted without the use of a desolvation chamber, except for the determination of Cl (see Chapter 5).

The desolvation system is shown in Figure 7 and was a modified version of that used by Galante et al. [20]. The system consisted of a heated pyrex tube to dry the aerosol and a 6 in long condenser with a spiral condensing tube (1 cm i.d. X 28 cm long) to remove much of the water vapor. The desolvation tube was wrapped in heating tape to maintain a tube temperature of 150^{o}C. The wrapped tube was then encased in an insulating outer pyrex tube (2 in i.d.), which also served to hold the heating tape in place. The condenser was maintained at a constant temperature of -10 ^{o}C by a refrigerated circulating bath. A solution of automotive antifreeze (70 % v/v) was used as the coolant.

The entire desolvation system was connected by 12/5 ball joints for experimental simplicity. A 25 mL conical flask was used for waste collection.

Microwave Cavity

The microwave cavity chosen for this work is diagrammed in Figure 8. The design is a modified version of that described by Boss, Madus, and Riddle [21]. Modifications

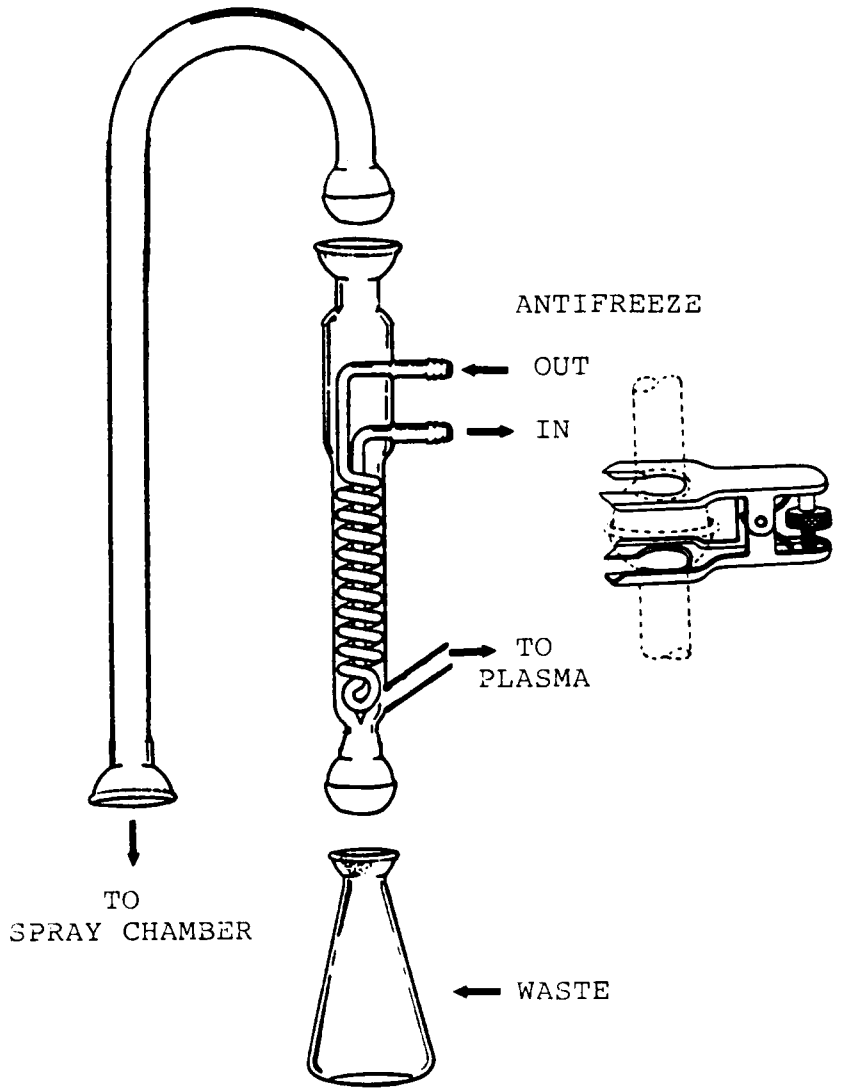

FIGURE 7: Diagram of the desolvation system.

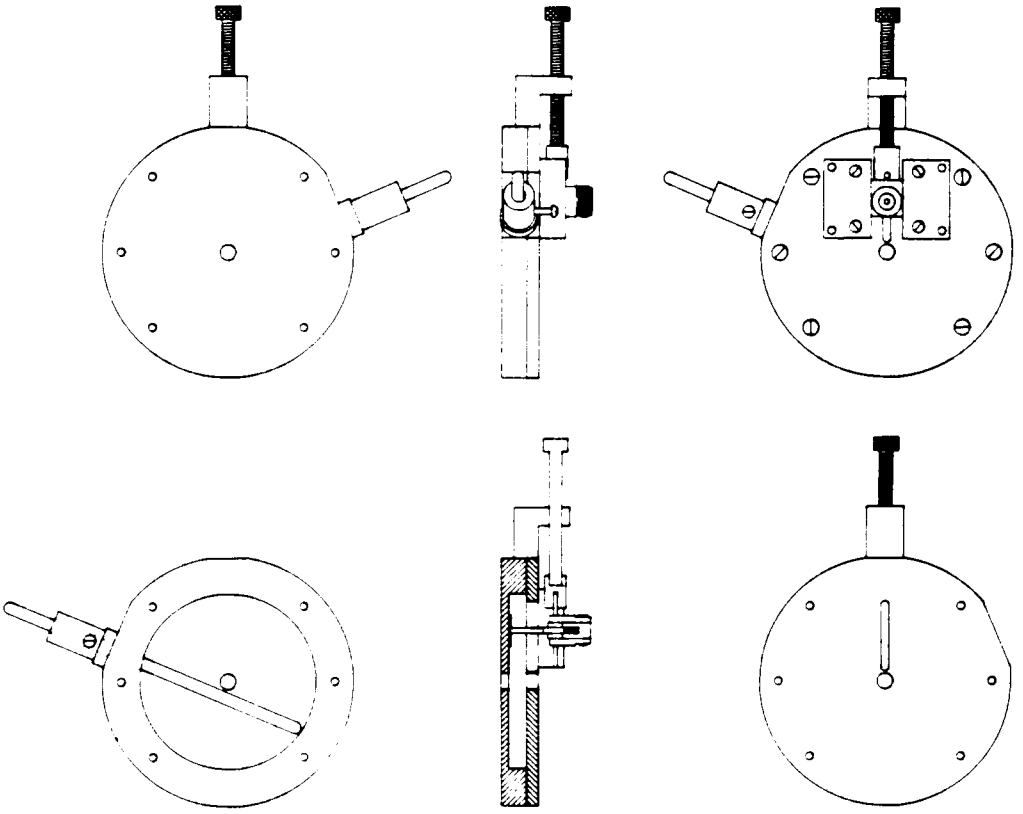

FIGURE 8: Schematic of the He-HEMIP.

included a change in size and reconstruction of the probe translation stage. The cylindrical cavity was machined from a 0.78-in thick sheet of oxygen-free high conductivity copper (OFHC). The internal diameter and depth of the cavity were fixed at 89.1 mm and 10 mm, respectively. A 6 mm diameter quartz rod extended into the cavity from the side wall. Movement of the quartz rod provided tuning of the cavity resonant frequency to the generator frequency, 2.45 GHz. A brass tuning rod extended into the cavity from the side wall opposite the quartz rod. This brass tuning rod was initially employed for frequency tuning. However, it was determined later that the brass rod was very ineffective in tuning the cavity and was removed.

A removable cavity lid was machined from a 0.197 in OFHC sheet. An 8 mm hole was drilled into the center of the lid to facilitate insertion of the plasma discharge tube. A 5 X 40 mm radial slot was milled along the coordinate axes of the circular lid. This allowed lateral movement of the capacitive antenna coupling probe.

The capacitive antenna coupling probe was used for proper coupling between the generator and the load (plasma). The capacitance of the probe was adjusted by varying the surface area at the end of the probe. Coupling was further adjusted by sliding the probe along the radial face of the

cavity to match the capacitive and inductive coupling power to match the impedence of the generator.

Antenna probes were fashioned from UG 58 A/U type N coxial connectors, as described by Boss [21,22]. A 10 guage copper wire was soldered to the center post of the N connector. A 16 mm diameter metal disk was soldered to the end of the copper wire. Sheet metal shims were used to set the probe penetration depth at 96%. The probe translation mechanism was constructed from brass.

Microwave Torch

A centered plasma was produced using a tangential torch similar to those currently employed in ICP-AES [23]. The torch used in all studies consists of two concentric quartz tubes (see Figure 9). The dimensions of the outer tube were 5 mm i. d., 8 mm o. d. and 9 cm long. The inner tube was 1.5 mm i. d., 2 mm o. d. and 2.5 cm long. For all experiments, the He flow was introduced tangentially into the outer tube along with the analyte aerosol from the nebulizer. This method of introduction allowed for a homogeneous mixture to form between the aerosol and plasma gas before ignition. The plasma uniformly filled the discharge tube and extended beyond the face plate of the cavity. Initially, aqueous samples were to be introduced through the center tube, however the back pressure created by the small center tube made this task impossible. Because

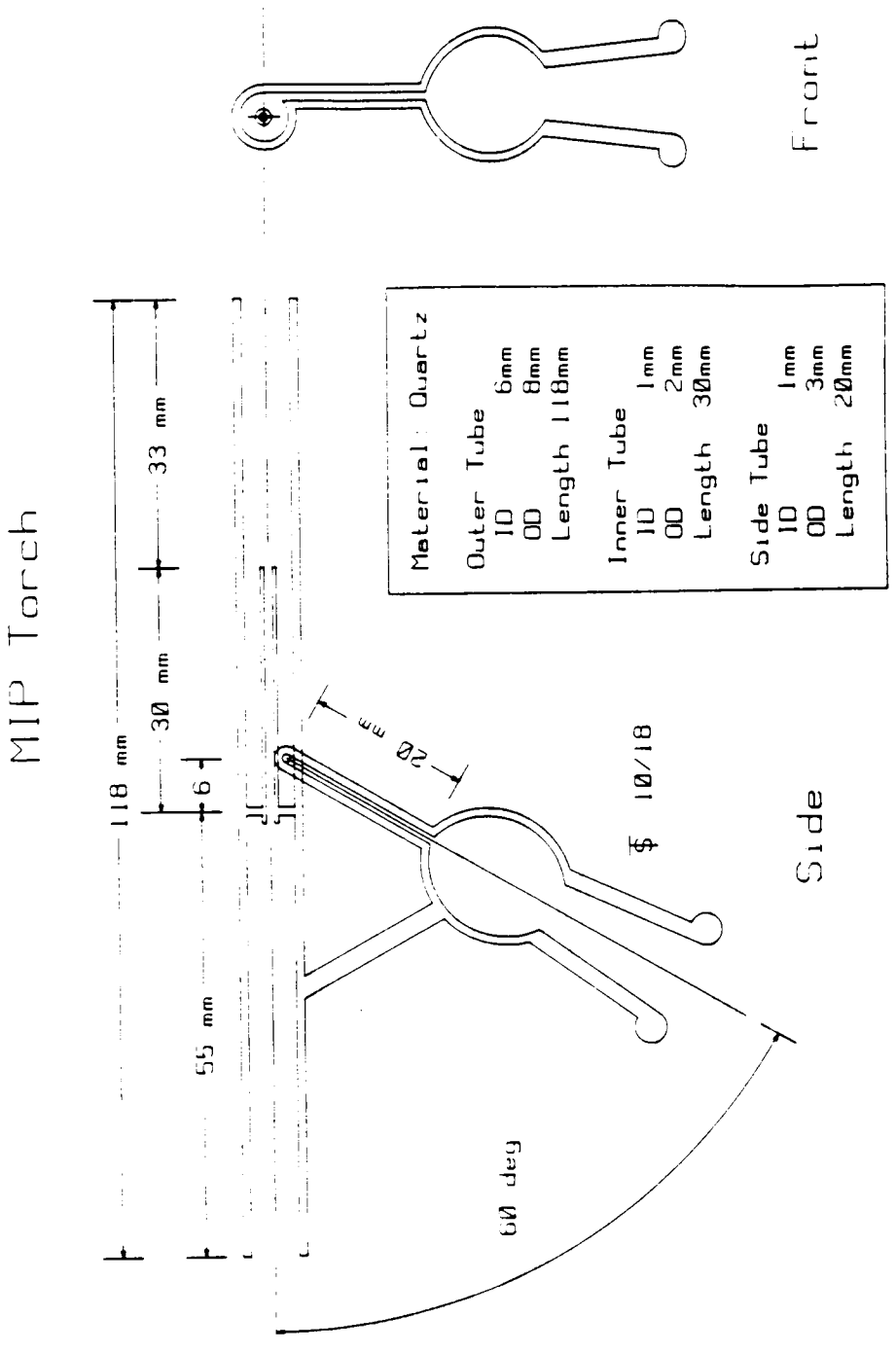

FIGURE 9: Schematic of the tangential flow torch for the He-HEMIP.

of the back pressure problem, the center tube was constricted using sealed tygon tubing to prevent leakage of the He plasma gas.

Plasma Ignition and Operation

In operation, the He-HEMIP is self-igniting. On those occasions when the plasma did not ignite the following procedure was employed. The circular probe was placed near the center of the cavity. The plasma gas was allowed to flow through the side inlet of the torch (i.e., 1-2 L/min). Microwave power was applied to the cavity, up to 150 W maxinimum. The quartz tuning rod was adjusted to obtain a minimum reflected power. The plasma was ignited with a small tungsten wire attached to a rubber policeman, whereby inductive heating of the wire caused a seeding of the He gas. If the plasma did not ignite, the probe was moved toward the walls of the cavity, and the above process repeated. Once the plasma ignited, the reflected power was minimized by adjustments of the antenna probe and quartz rod. The flow was reduced to 1 L/min, to sustain the plasma by the nebulizer alone.

The optimum operational parameters used for all studies are shown in Table 2.

TABLE 2: Operational Parameters

	AES	AFS
Forward Power	150 W	150 W
Reflected Power	0 W	0 W
Observation Height*	2-3 mm (+0.5 mm)+	8 mm
Nebulizer Uptake	0.46 mL/min	0.46 mL/min
Aux. He Flow	0 mL/min	0 mL/min
Total He Flow	1 L/min	1 L/min
Probe Penetration	96 %	96 %
Time Constant	3 sec	3 sec
HCL Power	-	10-25 mA

* Radial height above the top of the cavity.

+ Axial distance from the center of the cavity.

Plasma Behaviors and Features

Using the He-HEMIP, the He plasma was stable over all operating periods used to gather data. The time period varied from 30 min to 10 hours of plasma operation. Further tuning was not needed during these time periods. The temperature of the cavity did not exceed 35^{o}C.

After ignition, the tangentially formed plasma appeared red in color. A blue color formed the afterglow. Once aqueous samples were introduced, the intensity of the red color increased. When organic solvents were aspirated, a large greenish-blue afterglow formed, apparently, resulting from the combustion of organic species.

Limits of Detection

The limits of detection were all calculated in accordance with IUPAC guidelines using the following equation [24-26]:

$$c_L = (k*Sbk) / m$$

where c_L = limit of detection
k = confidence value
Sbk = standard deviation of the background
m = analytical sensitivity

For each limit of detection calculation, 20 background readings were taken. The analytical sensitivities were calculated from the working curves of the element, which spanned at least three orders of concentrative magnitude. The k value used for all calculations was 2, rather than 3. This lower k value was used only for comparative purposes with the existing literature.

Data Presentation. The data presented in this report are shown as background corrected values. For AES and AFS profiles, the background signal was subtracted by the computer from the analyte signals. Working curve and interelement effect plots were similarly treated.

Data sets for temperature and electron number density studies represent an average of at least five repeated experiments.

CHAPTER 3

PHYSICAL MEASUREMENTS OF THE He-HEMIP

Measurements of physical parameters play an important role in the development of any atomization source for spectrometric analysis. These measurements provide the information necessary for the determination of plasma properties such as electron number densities, particle energies, distribution temperatures, and gas-flow dynamics. In turn, these properties are used as a basis for describing fundamental processes or mechanisms related to interactions between analyte species (atoms, ions, and molecules) and plasma species (electrons, atoms, ions, and molecules).

In the strictest sense, a temperature may only be defined for systems in thermodynamic equilibrium, TE. The existence of such a state implies the fulfillment of several criteria [27]:

a) The velocity distribution function of all particles behaves according to Maxwell's equations.
b) The excited states are populated according to the Boltzmann distribution.
c) The distribution of the atom-ion equilibria behaves according to the Saha-Eggert relationship.

d) The distribution of molecules and their dissociation products behaves according to the mass action law of Guldberg and Wagge.

e) The distribution of electromagnetic radiation in the plasma must be in agreement with Planck's law.

Simply stated, a system is in TE if it can be described by a single temperature. Temperature in this sense is a descriptive term that relates the magnitude of each type of energy associated with the plasma. In an atomic gas, one recognizes several temperatures [27]:

(a) electron temperature, which is determined by the kinetic energy of electrons

(b) gas temperature, which is defined by the kinetic energy of neutral atoms

(c) excitation temperature, which describes the populations of the various energy levels

(d) ionization temperature, which governs ionization equilibria.

Summarizing, in an atomic gas one recognizes translation, excitation, and ionization temperatures. In molecular gases, temperatures assigned to dissociation equilibria and to rotational and vibrational states of the molecules should be added. In a plasma discharge, the numerical differences among the temperatures depends mainly

on the strength of the applied electric field (E) and on the gas pressure (P), actually on the ratio P/E. At reduced pressure and/or in a strong electric field the electron temperature is high, whereas the gas temperature is low. As the electric field is attenuated and/or the pressure is raised, the electron temperature decreases and the gas temperature rises. Finally all temperatures become numerically equal when the system has reached a state of thermal equilibrium.

Unfortunately, no laboratory plasma exists in a state of complete thermal equilibrium [28]. Since only the radiation field in a blackbody source follows Planck's distribution. The flame or plasma cannot be described by Planck's function because it is often transparent over large wavelength regions. Thus, radiation equilibria may only exist in the central portion of the flame or plasma source, and at the wavelength center of strong resonance lines. This lack of radiative equilibrium produces a depopulation of the upper energy levels with respect to the lower ones, because the atoms and molecules are deexcited by emission of radiation and inelastic collisions. Therefore de-excitation, since self absorption is relatively small, occurs only by inelastic collisions. Nonetheless, the extent of this depopulation effect is small for plasma

collisional induced transitions and are more frequent than radiative ones.

In cases for which the Planck function is not valid, all other relationships can remain locally valid. Plasmas satisfying these other relations at any spatial point, and at any instance in time, are said to be in local thermal equilibrium, LTE. Generally, laboratory plasmas and flames are described qualitatively and quantitatively in terms of their deviation from LTE. At atmospheric pressure, LTE would be expected to prevail in flames and plasmas because of their high particle density and collision frequency.

To evaluate whether a plasma is in LTE or non-LTE, the most important criteria are temperature and electron number density measurements. These measurements can provide the spectroscopist with insight on the reaction mechanisms occurring in the plasma. The experimental values of temperature and electron number density are directly related to the extent of departure from LTE, and are extremely helpful in characterizing the volumes of different species for analyte excitation.

In this chapter, diagnostic studies of the He-HEMIP are presented. Diagnostic measurements include excitation temperatures with the use of aqueous and organic nebulized thermometric species, electron number densities, and ionization temperatures for the plasma.

EXPERIMENTAL

The He-HEMIP was viewed in the radial mode for all measurements reported in this chapter, unless otherwise stated. A 1.0 mm circular aperture was positioned in front of the entrance slits of the monochromator upon which the radiation from the He-HEMIP was focused. A 25 um slit width was used, providing a spectral bandpass of 1.5 A, unless otherwise stated. The He-HEMIP was translated in the X, Y, and/or Z direction via translation stages (NRC).

All reported data are background subtracted. Data sets for temperature and electron number density studies represent an average of at least five repeated experiments. Abel inversions were not used for radial spatial information (see Chapter 2).

Electronic Excitation Temperature.

The electronic excitation temperature of the He-HEMIP was determined from the spectral emission intensities of helium and iron as thermometric species [28]. An iron solution of 1000 ppm was introduced into the plasma and the relative intensities of the iron atom lines in the spectral region of 370-390 nm were measured. Helium atom lines in the region of 380- 502 nm were also measured. The excitation temperature was determined from the following equation [29]:

$$\ln\left((I_{pq}/g_p)/(A_{pq}\ v_{pq})\right) = E_p/(kT)$$

where I_{pq} = measured relative intensity

g_p = statistical weight of the upper state

A_{pq} = transition probability

v_{pq} = frequency of the pq transition

E_p = energy of the upper state

k = Boltzmann constant

T = electronic excitation temperature

A plot of $\ln\left((I_{pq}/g_p)/(A_{pq}\ v_{pq})\right)$ vs. E_p yields a straight line with a slope inversely proportional to the excitation temperature [-1/(kT)]. Constants for all iron and helium lines used for temperature measurements are listed in Tables 3 and 4, respectively.

Ionization Temperature

The spatial ionization temperature, T_{ion}, was determined from the relative emission intensities of the cadium atom (228.8 nm) and cadium ion (226.5 nm) lines using the same position and resolution as the measurements for the excitation temperature, and was calculated using the following Saha-Eggert relationship [29]:

$$(I_i/I_a) = \frac{4.83 \times 10^{15}}{n^{e-}} (g_p A_{pq}/\lambda_{pq})_i\ (\lambda_{pq}/g_p A_{pq})_a$$

$$\times\ T^{3/2}\ \exp[(-E_i - E_{pi} + E_{pa})/kT]$$

Table 3: Wavelengths and Constants used for Iron Temperature Determinations

Wavelength (nm)	E_p (cm^{-1})	g_p	A_{pq}
370.5	27395	7	0.0328
372.2	27560	5	0.0505
373.5	33695	11	0.886
374.8	27560	5	0.0904
375.8	34329	7	0.611
382.0	33096	7	0.638
385.6	45295	11	0.87
389.6	49461	11	0.14
390.0	51771	7	0.086

Table 4: Wavelengths and Constants used for Helium Temperature Determinations

Wavelength (nm)	E_p (cm^{-1})	g_p	A_{pq}
388.87	185565	9	0.09478
447.15	191445	15	0.246
471.31	190298	3	0.0955
501.57	186210	3	0.1338

where I_i = intensity of the ion line

I_a = intensity of the atom line

g_p = statistical weight of the upper transition

A_{pq} = transition probability of the upper transition

λ_{pq} = wavelength

n^{e-} = electron number density

T = ionization temperature

E_i = ionization energy of the species

E_p = excitation energy of the upper transition

The Saha equation can be combined with the Boltzmann equation to relate intensities of line emission from the two charged species. While this equation has no exact solution for T, it can be solved numerically using a computer program written in BASIC (Appendix).

Electron Number Density

Three methods were used for the determination of the electron number density in the He-HEMIP:

(1) measurement of the Stark broadening of the hydrogen-beta Balmer line as described by Griem [30].

(2) the He line method also described by Griem [30].

(3) Saha-Eggert relationship method [29].

The determination of the electron number density by full-width at half height (FWHH) of the Stark broadening of the hydrogen-beta Balmer line (486.1 nm) tends to be the most common method. This line offers several particular advantages [28,30]:

(a) the range of half-widths anticipated (approximately 1.0 to 5.0 A), and the relative intensities are large enough to allow accurate measurements at various observation heights in the plasma.
(b) extensive Stark data are available for complete line profiles encompassing a broad range of electron number density values and temperatures.
(c) Stark broadening is strongly influenced by an electric field, making it a sensitive measurement
(d) the line is relatively temperature independent, with little variation over tens of thousands of degrees.
(e) it is relatively free from spectral interferences by plasma components.
(f) greater accuracy is generally associated with Stark calculations for the hydrogen beta line than for other atomic hydrogen lines [30].

After deconvolution of the line profile to account for instrumental, collisional and Doppler broadening, the

electron number density can be related to the FWHH by the following equation:

$$n_e = C(n_e,T) \left(\lambda_s \right)^{3/2}$$

where: $C(n_e,T)$ is a function of electron density and temperature

λ_s = FWHH of the hydrogen beta line.

$C(n_e,T)$ values are tabulated in Griem's book for different values of electron temperature and electron number density [30].

Experimentally, a spectral scan of the hydrogen beta line at 486.1 nm is all that is necessary for the electron number density determination. Broadening from the effects mentioned above is ordinarily small and is usually neglected. Calculations were performed using a BASIC computer program; see Appendix A.

The helium atom 388.9 nm line was also employed for the effective electron number density determination. Experimentally, this method follows that of the hydrogen-beta measurement. In contrast to the considerable amount of experimental data for hydrogen lines, there is very little laboratory material available for Stark-broadened lines from helium, the next one-electron sequence [30]. However, in view of the successes with

sources in the case of hydrogen lines, this should not be considered a drawback.

The electron number density can also be determined from the Saha-Eggert ionization relationship [29]. This method requires the determination of the relative emission line intensities from successive ionization stages, generally for the neutral atoms and ionized species. When these intensities are combined with the known equilibrium relationships between the emission spectra, temperatures and the Saha-Eggart expression, the electron number density can be obtained. Electron densities so obtained are dependant upon the assumption that the plasma is in LTE, which may not be the case.

Two elements, cadium and calcium with neutral atom ionization potentials were selected for atom/ion emission line intensity measurements. These elements were primarily selected for the following reasons:

(a) availability of transition probably data for atom and ion lines
(b) closely matched excitation energies for the atom and ion pairs so that the exponential temperature effect would be minimized
(c) freedom from spectral interferences
(d) freedom from physical and chemical interferences

(e) wavelength proximity so that the necessity of calibrating the detector response with respect to the wavelength could be circumvented [28,29].

The wavelengths, their excitation energies, statistical weights and transition probably data are given in Table 5.

RESULTS AND DISCUSSION

Excitation Temperature

The excitation temperatures were determined using several thermometric species (He with and without water, aqueous Fe and organic Fe) and are tabulated in Table 6. The temperatures varied from 5100 K (organic Fe nebulization) to 6100 K (radiance of He lines). It is interesting to note that the excitation temperature with the nebulization of water alone into the plasma, and the introduction of iron as the thermometric species into the plasma, resulted in values that were not statistically different. The random error for the estimation of the excitation temperatures is less than 90 K. The decrease in the excitation temperature for organic nebulization into the plasma, although not experimentally confirmed, can be attributed to the absorption of energy by molecular species (C_2, CN, CO, etc.) from the plasma. This type of phenomenon was also found to occur in the ICP, in which the temperature was lower for an organic aerosol than for an aqueous aerosol

TABLE 5: Data for Saha-Eggart Electron Number Density Calculation

Species	Wavelength (nm)	E_q (cm^{-1})	g_q
Ca I	422.7	23652	3
Ca II	396.8	23192	2
Cd I	228.8	43692	3
Cd II	226.5	44136	2

TABLE 6: Excitation Temperatures by Slope Method

Thermometric Species	Temperature (K)
He	6100
He + H_2O	5800
Fe (aqueous)	5600 (axial)
	5800 (radial)
Fe (Ferrocene)	5100

at a fixed power and observation height [31]. According to Blades, the molecular carbon species adsorb energy from the plasma and affect the thermal conductivity of the plasma during the process of dissociation. It should be noted that this effect of lowering the excitation temperature by the nebulization of organic liquids into the He-HEMIP is smaller than that found for a 1.75 kW ICP, where a reduction in the excitation temperature by the nebulization of organics was found to be approximately 1500 K [31].

A comparison of the excitation temperature of the He-HEMIP used for this work and that of other plasma sources are shown in Table 7. The results of this comparison show that the excitation temperature of the He-HEMIP is higher. This increased excitation temperature is a indication of the robustness of the He-HEMIP and is also an indication that this plasma source may be closer to LTE than any other previous microwave cavity.

Ionization Temperature

Spatially integrated intensities of the cadium emission atom (228.8 nm) and cadium ion (226.5 nm) lines were measured for the determination of the ionization temperature. Results of the ion/atom line ratios were tabulated and substituted into the Saha-Eggert relationship and T_{ion} calculated using an iterative process. T_{ion} as determined by the Saha-Eggert equation was 6200 K.

Table 7: Excitation Temperature for Serveral Helium MIPs

Operating Power (W)	T_{exc}	Reference
130	4500	32
75	3400	33
75	6000	34

Electron Number Density

Figure 10 depicts the electron number density, n_e-, profile across the face of the cavity, with and without direct nebulization of water at 0.46 mL/min, as determined by the half width from the broadening of the hydrogen-beta Balmer line at 486.1 nm. These number density determinations are at best an approximation due to the resolution of the monochromator employed. However, one feels that these relative values are useful in illustrating an n_e- trend with the introduction of samples into the plasma. The electron number density profile was demonstrated to be essentially flat with increases at 0.5 mm - 1mm without the nebulization of water. With the introduction of water by nebulization, the number density profile continues to increase above 0.5 mm, peaks at 1 mm, and levels off at 1.5 mm - 2.5mm. This increase in the number density with water nebulization may be the result of the ionization of hydrogen and oxygen species in the plasma. Since the ionization energies of hydrogen and oxygen are about 2 eV below those of argon, their degree of ionization at 6000 K would be expected to be about five times higher than that of argon thus an increase in the electron density would be expected when water is present [35-37].

Although the plasma visually appeared symmetric, the number density profile suggested that the plasma is

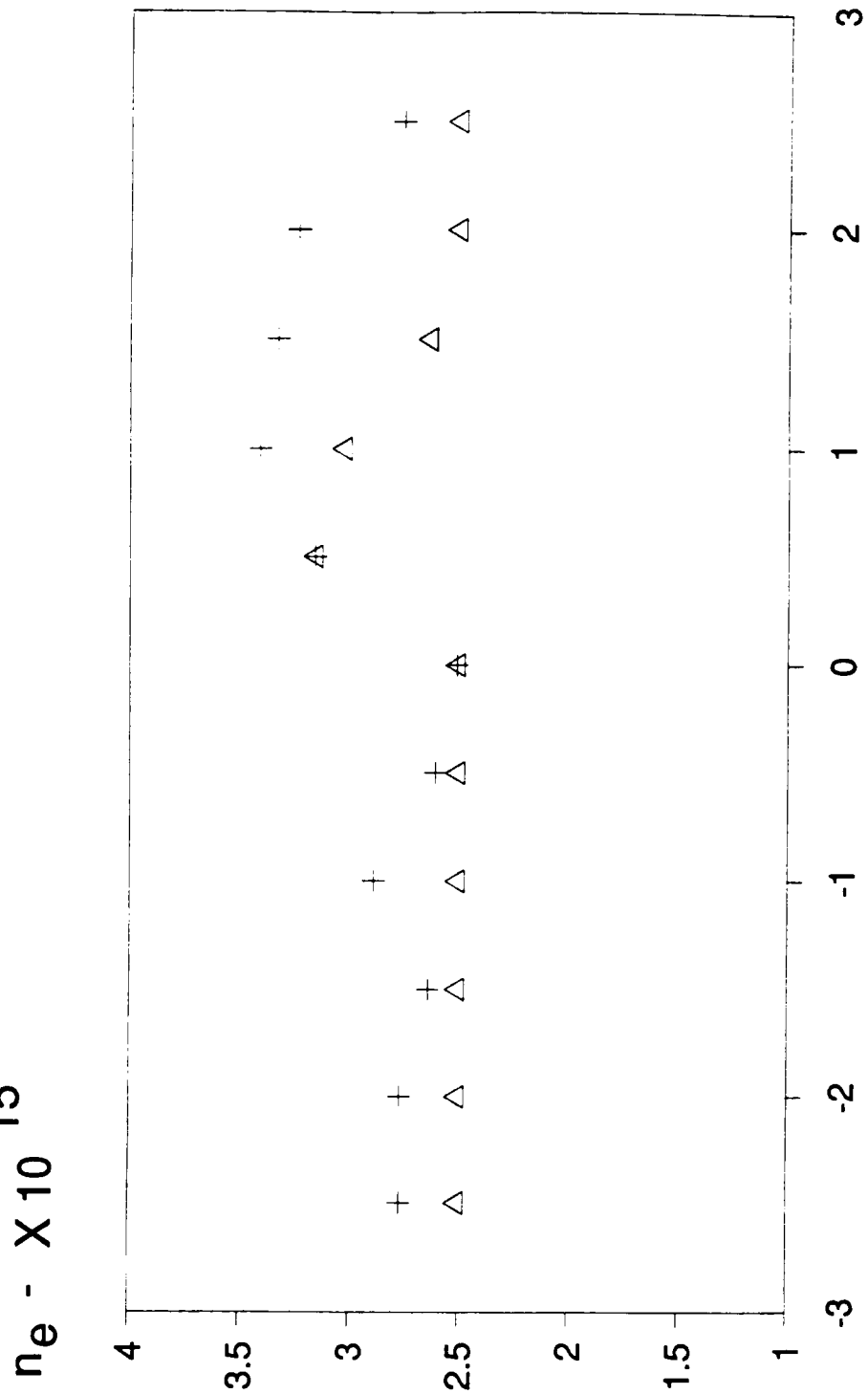

FIGURE 10: Spatially intergrated electron number density profile, with (+) and without water (Δ).

asymmetric. This asymmetry is attributed to errors in the flow pattern of the laboratory constructed torch. These errors in the flow pattern may be creating a hot spot in the plasma. To confirm this hypothesis, plots of analyte emission vs. observation heights for a variety of elements were constructed. In Figure 11, a representative plasma emission profile is shown. In this profile, the existance of an increase in relative emission intensity is observed at 0.5 mm - 1.0 mm in the plasma. This observation is the same as observed with the electron number density profile, suggesting the creation of a hot spot in the plasma.

The average n_e- using the helium line at 388.7 nm was determined to be 1.4 X 10^{14} e^-/cc and 2.5 X 10^{15} e^-/cc while employing the Saha-Eggart relationship.

CONCLUSIONS

The helium high efficiency microwave induced plasma approaches local thermal equilibrium (LTE). Evidence of this is based on the fact that the excitation temperature is approximately equal (within statistical error) to that of the ionization temperature. Unfortunately, without the knowledge of plasma gas temperatures, electron temperatures, an accurate electron number densities, the existence of LTE cannot be conclusively confirmed or rejected. The temperatures determined in this work and the ability to

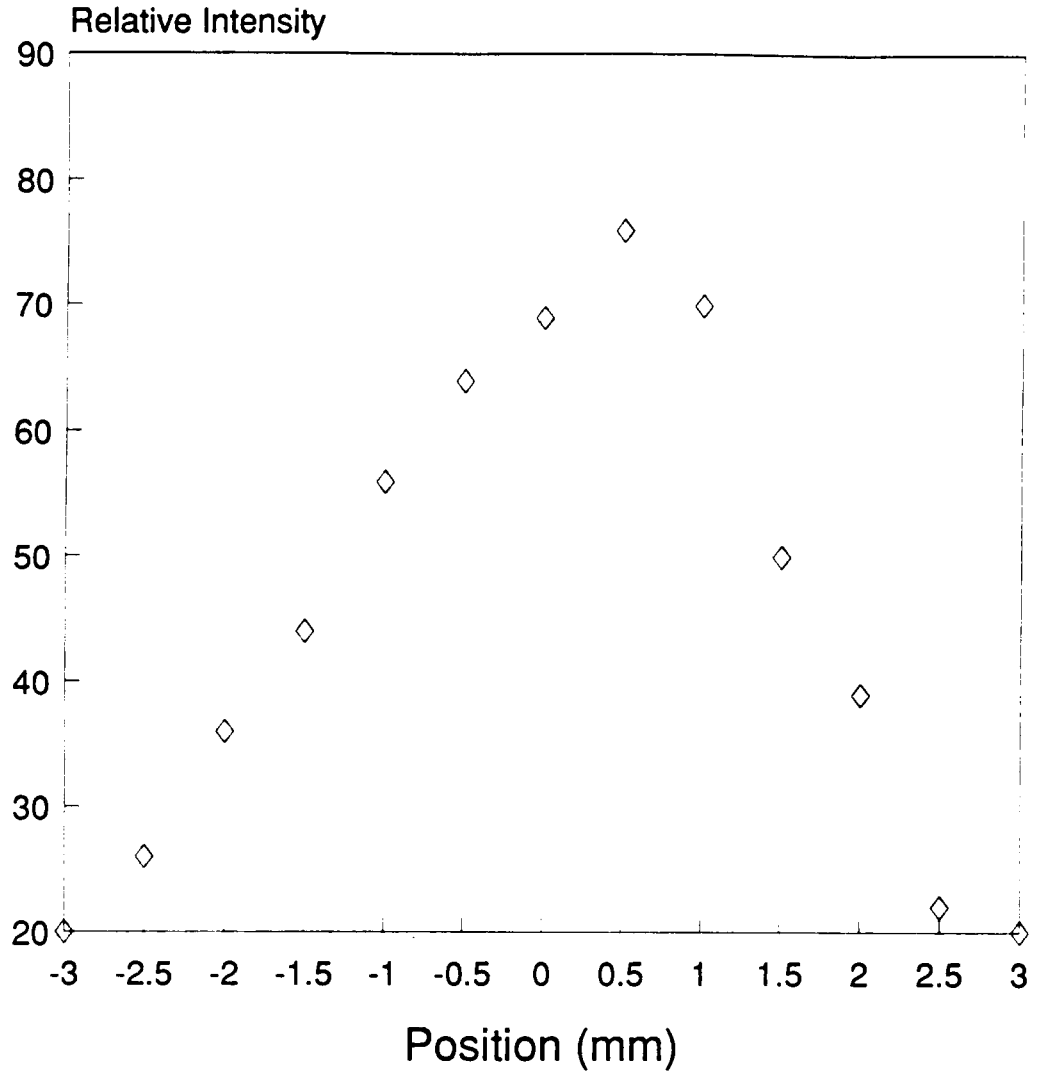

FIGURE 11: Spatial iodine emission profile of intensity vs. position.

directly aspirate organic samples directly into the He-HEMIP suggest that this source is the most robust of the MIP's used in the analytical community to date.

Chapter 4

Determination of Aqueous Metals by MIP-AES and MIP-AFS

The MIP has received considerable attention as an excitation source for atomic emission spectrometry since the introduction of the Beenakker cavity in 1976 [16]. The attractiveness of this cavity lies in its ability to operate at low power, at atmospheric pressure, and to support plasmas of various gases. These gases include argon, helium, nitrogen, and air. Although all of these support gases have found their analytical utility, helium seems to be of particular importance because of its high ionization potential, 24.6 eV. In addition, helium offers a simpler overall background spectrum, higher metastable energy, a greater optical transparency at shorter wavelengths and the capability to excite nonmetals and halogens. Primarily, gas phase sample introduction into the helium microwave plasma is of common practice. Over the past ten years, few reports have appeared on the use of direct nebulization of aqueous samples for the determination of metals and nonmetals in the helium microwave induced plasma [38-40]. This exiguity of studies with direct nebulization into the helium MIP focuses on the fact that the original Beenakker cavity does not afford sufficient desolvation and excitation of liquid samples. However, direct nebulization of metal and nonmetal

solutions into the helium plasma has been acheived using the Caruso type "two-stub internally tuned" cavity [41]. Carnahan and co-workers introduced aqueous chlorine, bromine, and iodine samples via direct nebulization using helium as the support gas. Power levels ranged from 500 W to several kilowatts, with plasma gas flow rates up to 50 L/min [39,40,42]. Detection limits employing UV-visible lines were obtained at and below one part per million.

This use of large power levels and gas flow rates clearly diminishes the low power advantages of the MIP (i.e., simplicity, versatility and low cost). Furthermore, the use of high power levels requires cooling (due to excessive heating of the cavity), and the utilization of special discharge tubes, with the expense of increased background emission, microwave leakage, and cost.

This chapter focuses on the use of a helium high efficiency MIP, He-HEMIP, for the determination of metals using direct nebulization. The HEMIP was developed by Matus et al. as a modification of the original Beenakker cavity, and precludes the use of external matching devices [21,22]. Instead, a capacitive antenna probe is used for proper coupling. The capacitance of the probe is adjusted by varying the surface area at the probe's end. Coupling is further adjusted by sliding the probe along the radial face of the cavity to match the capacitive and inductive coupling

of power with the impedance of the microwave generator. The power transfer efficiency was determined to be greater that 90% [21].

Using this cavity, Long and Perkins were able to sustain a centered and stable 1 L/min Ar plasma at 36 W, while nebulizing 1 mL/min of water without the use of desolvation apparatus [43]. In another study, Perkins and Long evaluated the use of this cavity as an atomization cell for atomic fluorescence spectrometry, using hollow cathode lamps and the Xe-arc as excitation sources [44]. Furthermore, the HEMIP tends to be more amendable to the introduction of directly nebulized aqueous and organic solutions, when compared to Beenakker cavities introduced to date [42,45].

Metal species were determined in the UV-visible region using atomic emission and atomic fluorescence spectrometry. No desolvation apparatus was employed.

Measurements of excitation temperatures, electron number densities, detection limits for AES and AFS, interelement effects, linear ranges, plasma profiles, and sample uptake studies are discussed.

EXPERIMENTAL

Instrumentation

A 25 um slit width providing a spectral band pass of 1.5 A was used unless otherwise stated. All operational conditions used were described in Chapter 2.

Studies of metal atomic emission and atomic fluorescence were conducted with the plasma in the radial position (side-on), unless otherwise stated.

RESULTS AND DISCUSSION

Effect of Sample Uptake Rate

Due to changes in solution viscosities, the effect of the sample uptake rate on atomic spectrometric signals is a very important parameter in system optimization. The effect of varying the aqueous solution uptake rate on the Ca (II) emission signal at 393.6 nm is shown in Figure 12 for a 50 ppm solution. The sample uptake rate was controlled by a peristaltic pump (Cole Palmer, Chicago, IL).

Little variation in the emission signal appears at a solution uptake rate of 0.17 mL/min up to 0.60 mL/min. Above 0.60 mL/min the signal rises by 17% and levels off between 0.80 mL/min and 1.0 mL/min. This data suggests that using this system there are no advantages in the use of a

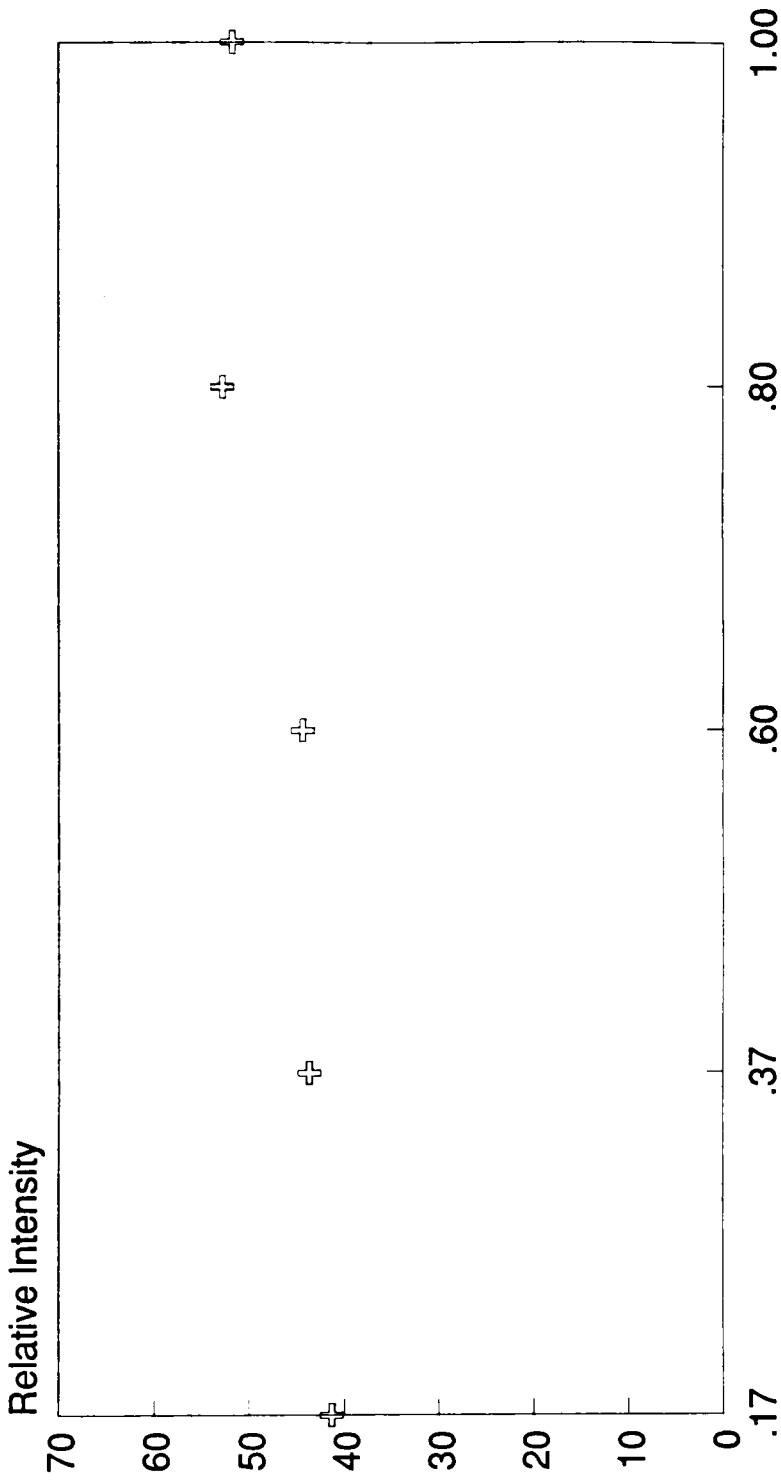

FIGURE 12: Effect of the sample uptake rate on the calcium emission intensity.

peristaltic pump compared to allowing the natural uptake rate to occur (0.46 mL/min).

Organic Nebulization

It was determined that the He-HEMIP can operate continuously (solutions with concentrations to 1000 ppm Ferrocene in xylenes: concentrations above this were not studied) during direct nebulization of organic samples. Carbon deposits on the torch wall were minimal and did not disturb the plasma.

The ability of the plasma to support organic nebulization at 0.46 mL/min without extinction by the organic aerosol indicated the He-HEMIPs robustness, as compared to other MIPs which have been used as chromatographic detectors in which must be vented, cooled or heated to prevent extinguishing of the plasma [46].

Profiles

Figure 13 depicts intensity profiles for AES and AFS using the optimized conditions outlined in Chapter 2 and a 6 mm i. d. discharge tube. For all AES studies for metal determinations, the optimum height was 2-3 mm above the top of the cavity. The optimum observation height for AFS measurements shifted to 8 mm above the top of the cavity. This shift in the AFS maximum intensity above that of the AES observation zone is consistent with earlier studies

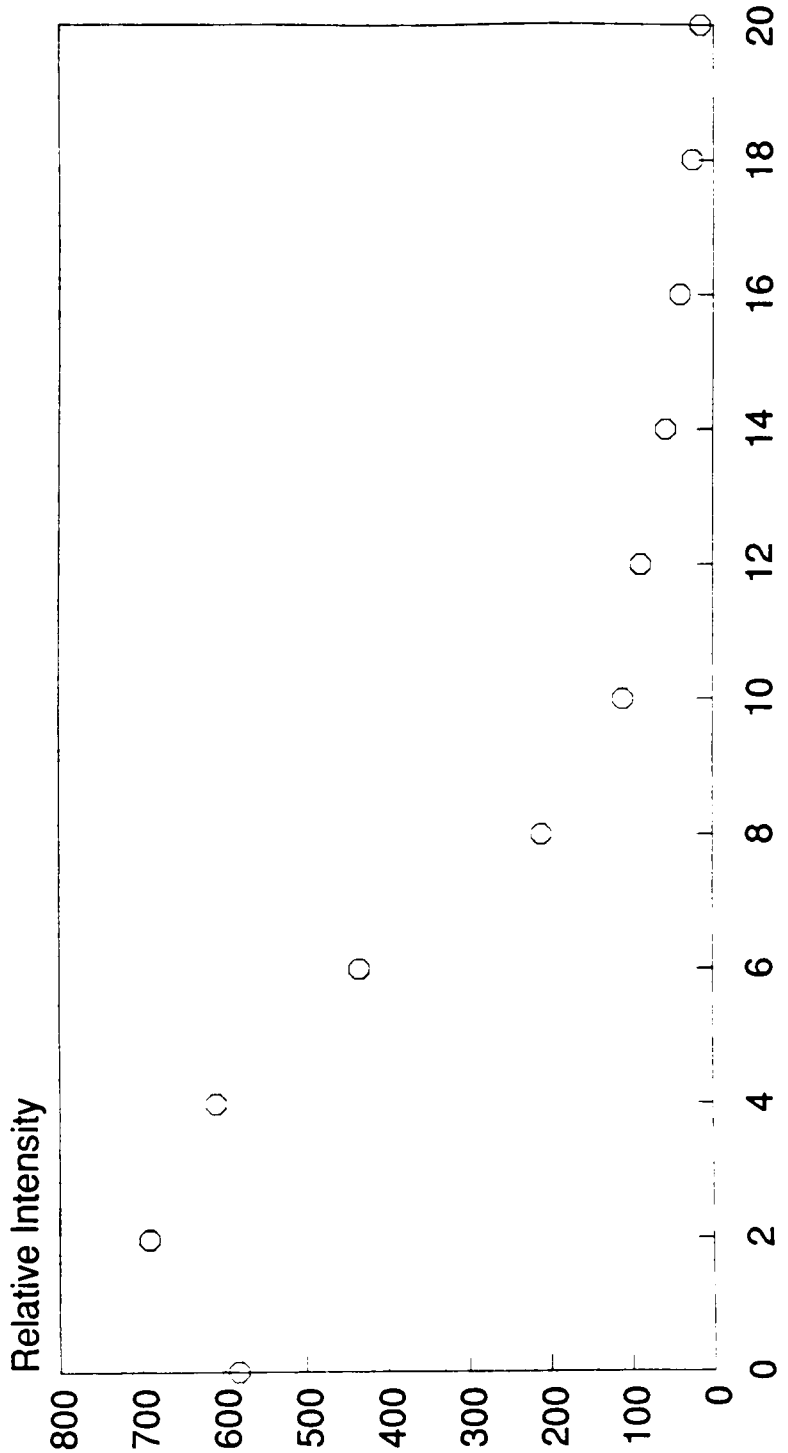

FIGURE 13: Radial emission profile for a 50 ppm calcium solution. Zero millimeter represents flush with the top of the cavity.

performed with the Ar-HEMIP [44]. In this higher region of the plasma there exists a decrease in plasma flicker and spectral background. In addition, the analyte species have experienced a longer residence time, resulting in a more complete molecular dissociation of the original species.

Linearity

The linearity ranges obtained for metal determinations using MIP-AES (radial mode) typically span four to five orders of concentrative magnitude. However, linear ranges for AFS span five and one-half orders of concentrative magnitude.

Limits of Detection

The limits of detection for metals using the He-HEMIP are listed in Table 8. These values were obtained for AES and AFS using direct sample introduction via a Meinhard nebulizer, and were calculated according to IUPAC standards [26]. It should be noted that a k equal to 2 was used, instead of the prescribed value of 3 as recommended by IUPAC. This substitution was done in order that the experimental detection limits could be compared to existing limits of detection for MIP and ICP systems.

The superior atomization characteristics of the He-HEMIP are compared to the Ar-HEMIP as shown in Table 8. In the first column of this table, the detection limits of

TABLE 8: MIP-AES Metal Detection Limits in ppb (k=2)

Element	λ (nm)	MIP-AES He	MIP-AES[a] Ar
Ag	328.1	7	120
Al	396.2	130	1400
Ba	553.5	-	180
Li	570.8	-	43
Ca(I)	422.7	5	40
Co	240.7	50	1800
Cr	357.9	70	8000
Fe	248.3	30	650
K	766.5	-	24
Mg	285.2	6	630
Mn	279.5	11	6900
Na	589.0	1	2
Sr	460.7	11	25
Zn	213.9	8	420

[a] Reference 43.

the MIP are shown for metal determinations using Ar and helium as support gases. The Ar data are from previous research with this cavity [43]. In all cases, except for Na, the use of He resulted in a substantial decrease (factor of 8 to 100) in the detection limit value. This trend is also observed for AFS data (Table 9), where the use of He for hollow cathode lamp (HCL) MIP-AFS resulted in a decrease in the detection limit from a factor of 4 up to 50. It should be noted that the current He-HEMIP limits of detection are not statistically different from that published for HCL-ICP-AFS [47].

Interelement Effects

The effect of the presence of an easily ionized element (EIE) on the Ca (I) atomic emission and fluorescence signal at 422.7 nm is shown in Figures 14 and 15. Using the conditions outlined in Chapter 2 and a 10 ppm Ca solution, no discernible effect of the Na interferent was observed to occur for AFS. However, a slight enhancement was observed for AES while introducing a 1000 ppm solution of the interferent, Na. The EIE effect in this He-HEMIP was significantly less than that observed using the Ar-HEMIP, where an increase in signal of 300% was observed for AES and 100% for AFS with a 1000 ppm Na solution [44].

Importantly, as shown in Figures 16 and 17, the classical phosphate interference was not observed for AES

TABLE 9: MIP-AFS Metal Detection Limits in ppb (k=2).

Element	λ(nm)	HCL-MIP-AFS He	HCL-MIP-AFS[a] Ar	HCL-ICP-AFS[b]
Ag	328.1	10	40	2
Al	396.2	80	700	20
Ba	553.5	8	20	50
Li	570.8	1.2	20	0.4
Ca(I)	422.7	1.7	20	0.4
Co	240.7	19	100	3
Cr	357.9	40	2000	8
Fe	248.3	30	600	10
K	766.5	1	20	0.8
Mg	285.2	1.3	20	0.5
Mn	279.5	-	500	3
Na	589.0	0.1	10	0.3
Sr	460.7	5	20	2
Zn	213.9	1.2	40	0.4

[a] Reference 43.

[b] Reference 47.

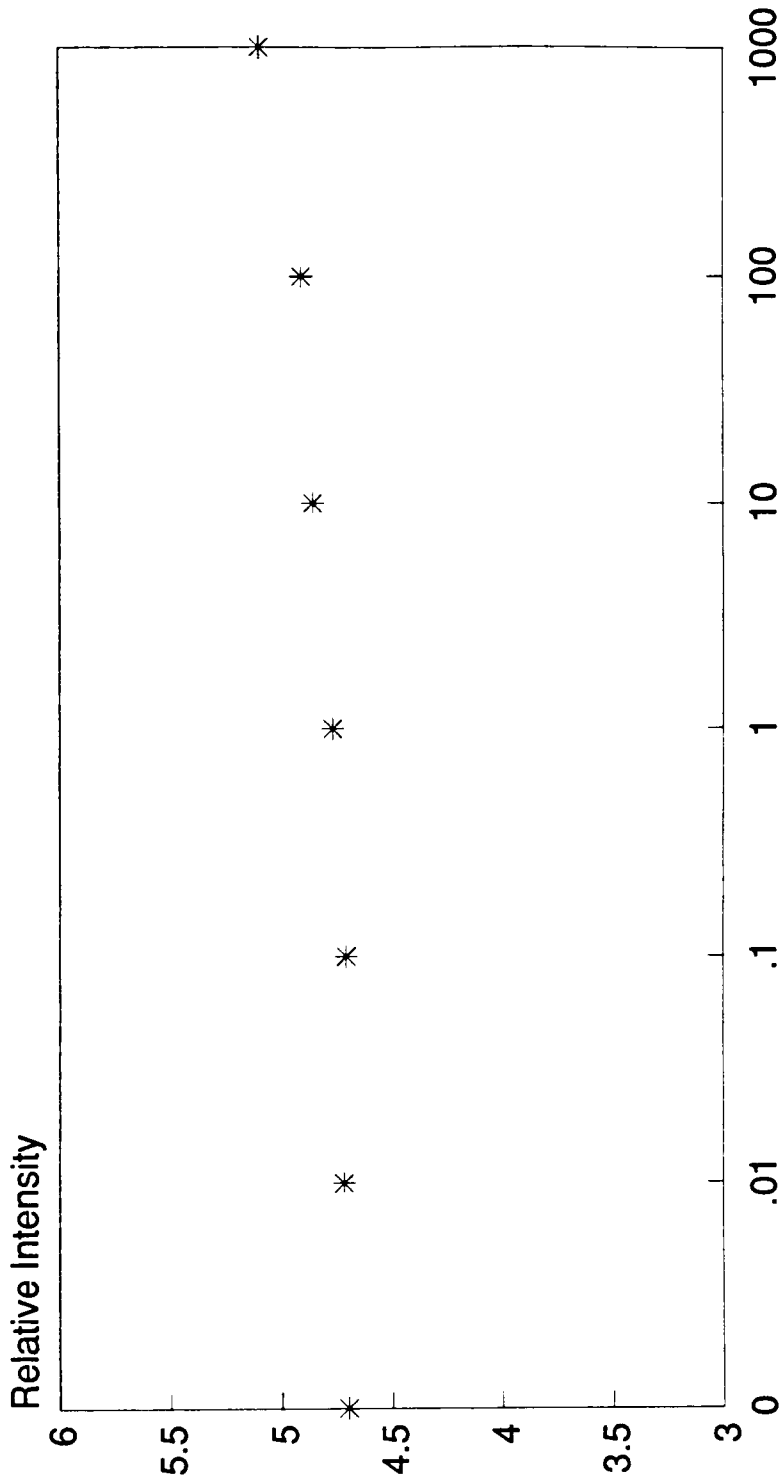

FIGURE 14: Effect of Na on the emission signal of a 10 ppm calcium solution.

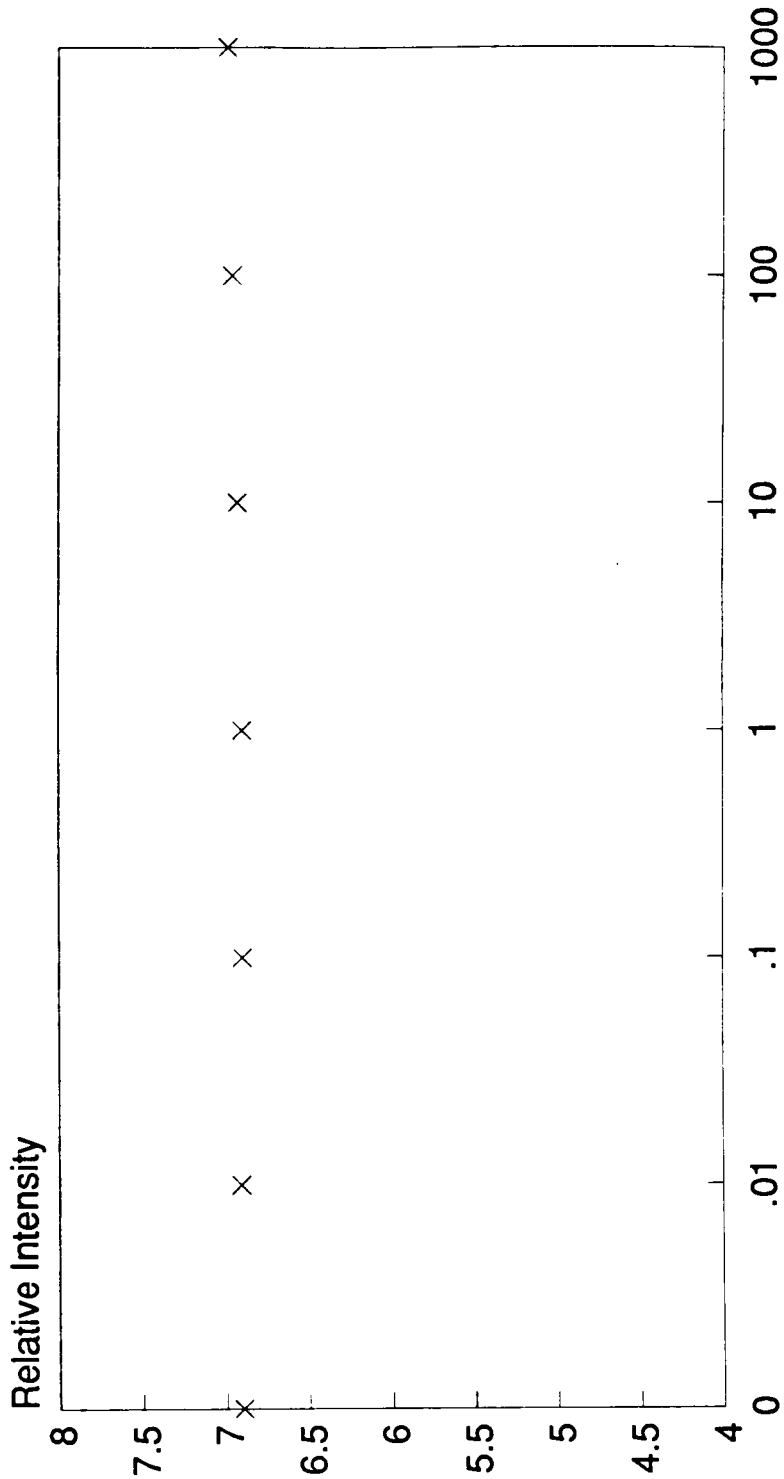

FIGURE 15: Effect of Na on the fluorescence signal of a 10 ppm calcium solution.

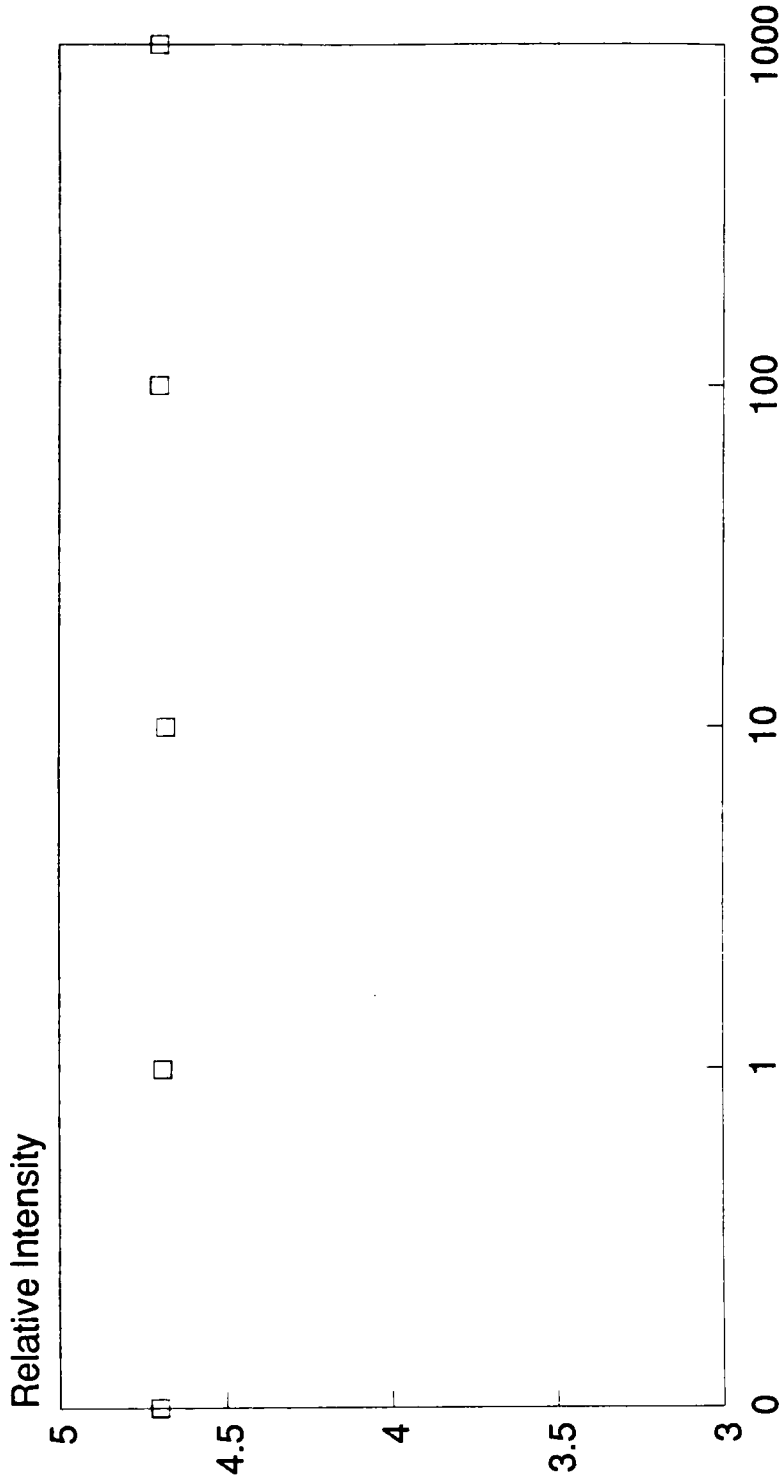

FIGURE 16: Effect of phosphate on the calcium emission signal (calcium concentration = 10 ppm)

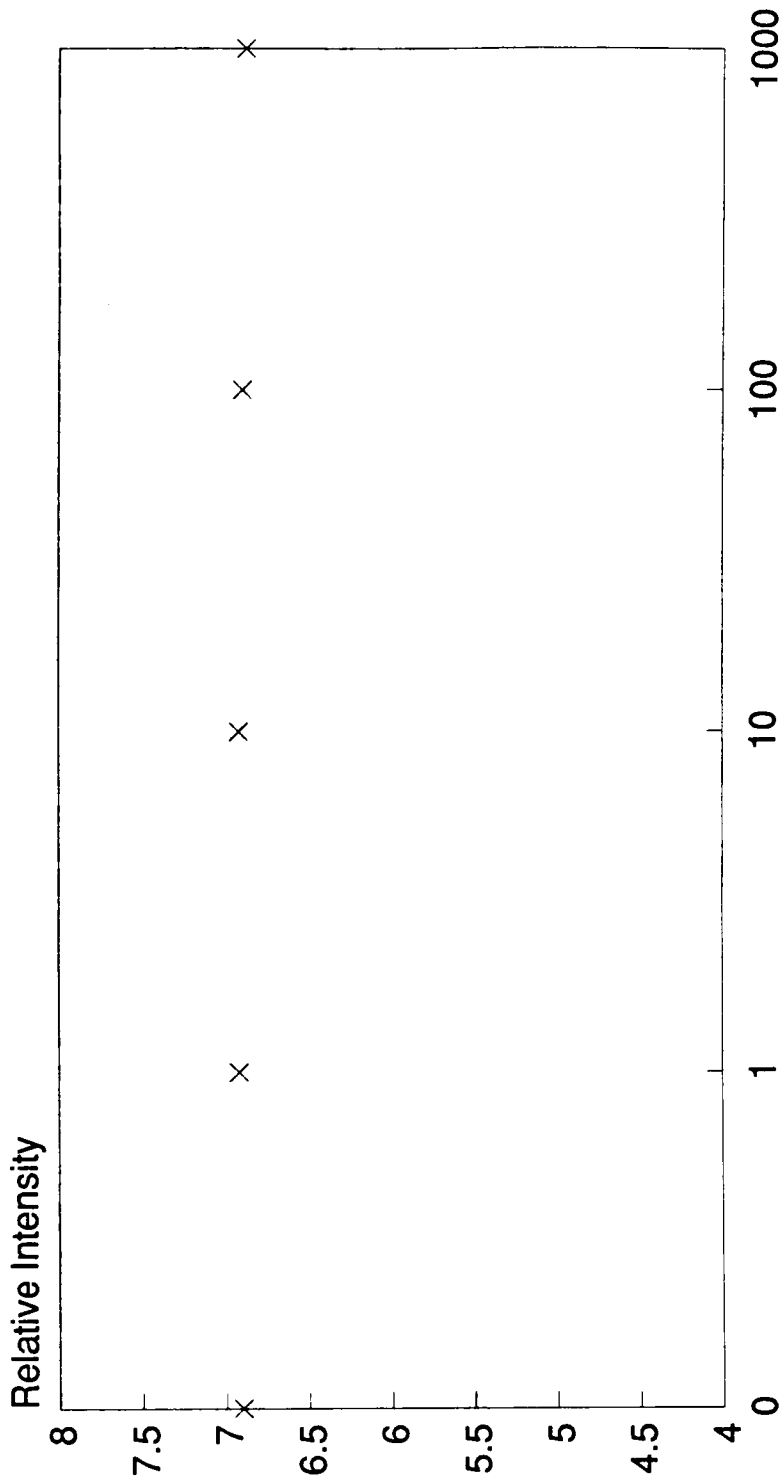

FIGURE 17: Effect of phosphate on the calcium fluorescence signal (calcium concentration = 10 ppm)

nor AFS. This suggests that the He-HEMIP is a robust atom cell that is able to efficiently cause complete dissociation of gaseous refractory molecules into free vapor phase atoms.

CONCLUSION

In this work, the advantages of using He versus Ar as the plasma gas for the high efficiency MIP with direct aqueous sample introduction for metal determinations by AES and AFS have been demonstrated. Not only were detection limits superior to that of Ar-HEMIP, but the values obtained for He-HEMIP-AFS are now equivalent to those of HCL-ICP-AFS. The robustness of He-HEMIP over Ar-HEMIP has been shown by the larger excitation temperatures, electron number densities and the freedom from interelement effects.

Chapter 5

Determination of Nonmetals by MIP-AES

Several well known methods exists for the determination of nonmetals in aqueous solution. These methods are: gravimetric, titrimetric and electrochemical (i.e., potentiometric titration and ion selective electrodes).

Gravimetric methods for the determination of Cl, Br, I, S, F, and P have been extensively studied [48]. Chloride, bromide, and iodide are determined by precipitation of their silver salts: AgCl, AgBr, and AgI, respectively. The sulfur in sulfides, sulfites, thiosulfates, and tetrathionates are determined by oxidizing the sulfur to sulfate and then precipitating barium sulfate. Fluoride is often determined by precipitation as CaF_2 and PbClF. Phosphate is determined by precipitation as $MgNH_4PO_4 \cdot 6H_2O$ [49].

With proper technique and ultmost care, gravimetric determinations have great accuracy. For example, if the analyte of interest is a major constituent (>1% of the sample), accuracy of a few parts per thousand can be expected if the sample is not too complex. If the analyte is present in minor or trace levels (<1%), a gravimetric method is not generally employed [49].

In general, gravimetric methods are not specific and are time consuming [50]. More over, potential problems of

coprecipitation, postprecipitation, improper technique, or incomplete reaction may lead to significant decreases in accuracy.

Titration methods are considerably more rapid than gravimetric methods because no lengthy drying (and/or ignition) and weighing steps are required.

Perhaps the most classical of all titrations is the determination of chloride with a standard solution of silver nitrate [51]. Bromide, iodide, and sulfate can also be determined offering increased accuracy than those of gravimetric methods. Limitations of this method includes the lack of suitable indicators, interferences from species that react with the titrant, and/or poor technique [48]. As with gravimetric methods, titrimetry is not well suited for ultratrace analysis [48].

The method of potentiometric titrimetry offers a number of advantages. Perhaps the primary advantage of potentiometric titrations is that (with the addition of classical titration procedures) they generally offer a large increase in accuracy and precision; +/- 0.1% levels are not uncommon [48]. Potentiometric end-point detection is applicable to chloride, bromide, and iodide. There are, however, certain disadvantages to potentiometric titrations: the increase in analysis time and operator attention required, and the difficulties associated with the

preparation, standardization, and storage of standard titrant solutions [51].

Ion-selective electrodes are especially useful for the determination of chloride, sulfide, bromide, iodide, and fluoride in aqueous solution [52]. The working range is quite large, generally from four to six orders of magnitude. Electrodes function well in colored or turbid samples. Analysis times are are reasonably rapid, with equilibrium being reached in less than one minute, but in some cases, usually in very dilute solutions, slow electrode response may require fifteen minutes to a hour for equilibrium. The equipment is simple and inexpensive. The method is non-destructive. The greatest disadvantage of ion-selective electrodes are that they are subject to rather large number of interferences. Ion-selective electrodes are not utra-trace level sensors; some electrodes are good down to only about 10^{-4} M, and are not usable around 10^{-6} M.

While it is clear from the above discussion that no universally sensitive and selective detection system exists for the determination of trace halogens, plasma atomic spectrometry shows great promise in this area. However, few reports concerning the application of this technique have appeared.

Direct analyses of nonmetals in solution have been performed by observing spectral lines in the vaccum

ultraviolet region of the spectrum with the inductively coupled plasma (ICP) [53]. While detection limits appeared promising, 1, 3, and 10 ppm for I, Br, and Cl, operation in the vacuum UV spectral region imposes constraints which may not be easily overcome. Vacuum monochromators and nonadsorbing optics must be used in all spectral determinations. Detection limits in the near infrared region were considerably greater, at 2000, 100, and 500 ppm for F, Cl, and Br [53].

Michlewicz and Carnahan directly nebulized nonmetal halide containing solutions into a high power (500 W) helium MIP [39,40]. They used emission lines in the UV-visible spectral region, and reported detection limits of 2 ppm for Cl, 60 ppm for Br, and 7 ppm for I [40]. However, the plasma required a modified resonator cavity, a specalized torch design (lifetimes less than 0.7 hour), 17-21 L/min of helium and an air coolant flow rate of 19-25 L/min. Moreover, an ultrasonic nebulizer and a desolvation system were needed to minimize the water loading of the plasma in order to achieve detection limits of 0.4 ppm for Cl, 3 ppm for Br, and 0.8 ppm for I. Their plasma also suffered from considerable matrix interferences, despite its high operating power.

In this chapter, the high efficiency helium microwave induced plasma (He-HEMIP) is explored for the determination

of nonmetals in aqueous solution. The He-HEMIP is more easily tuned and more resistant to solvent loading than are conventional Beenakker type cavities. Moreover, the He-HEMIP operates at low power and at a low gas consumption rate, thus producing lower overall background radiation, less microwave leakage and a longer residence time for the analyte in the optical path.

EXPERIMENTAL

All organic solvents were spectral grade. A list of the solvents used for nonmetal analysis are shown in Table 10. Aqueous standards were prepared using the procedure outlined in Chapter 2. Operational parameters and equipment were the same as outlined in Chapter 2.

RESULTS AND DISCUSSION

Wavelength Calibration

The selection of the sensitive spectral lines for organic vapor nonmetal determinations was achieved using the apparatus shown in Figure 18. The device termed "wavelength calibrator" was a modification of that used by Barnett and Kirkbright [54]. Modifications of the apparatus of Barnett and Kirkbright included changes in apparatus size and experimental procedure. The flask used in this study was 25

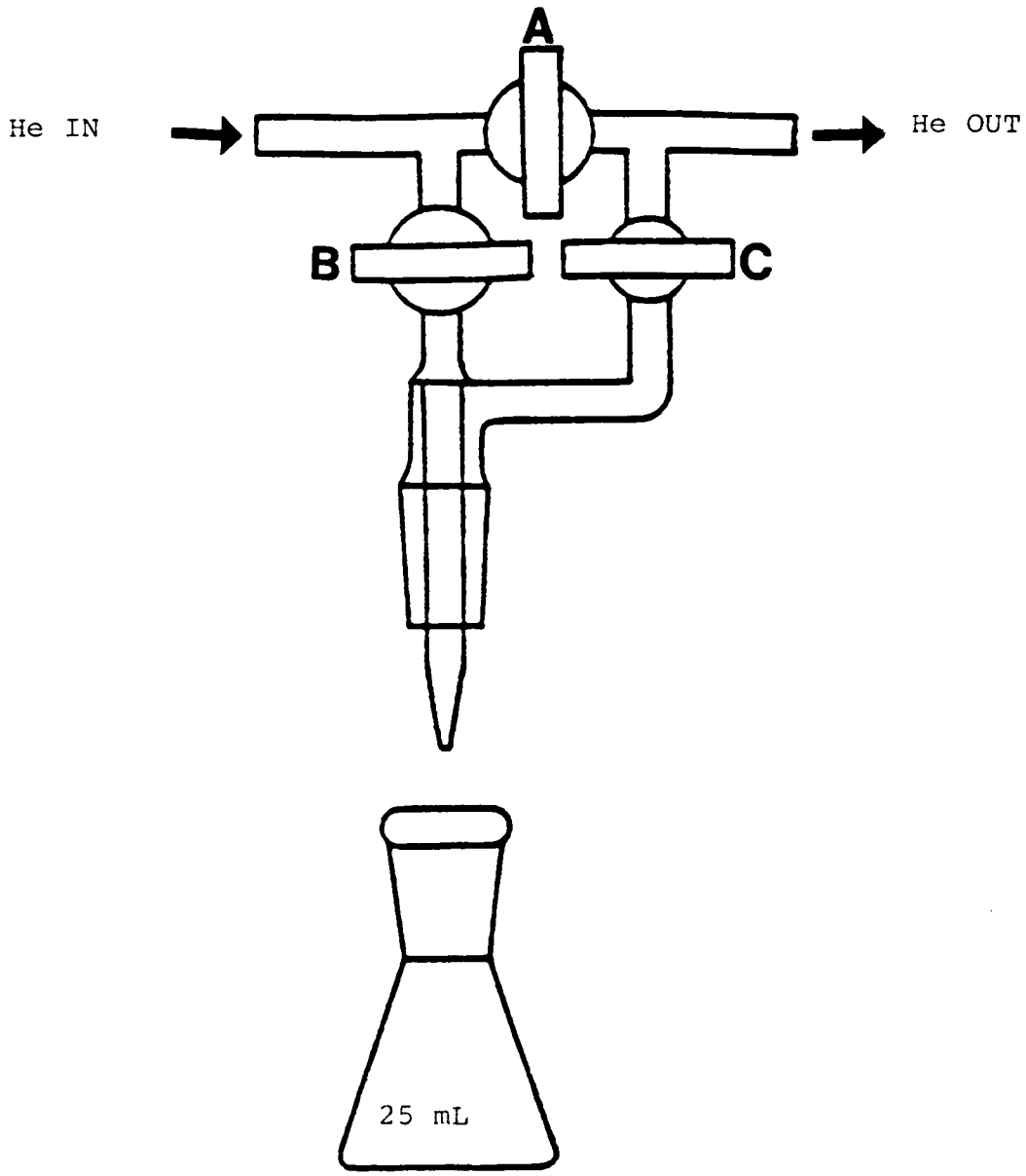

FIGURE 18: Wavelength Calibration device used for MIP-AES of nonmetals (From Ref. 54).

Table 10: Organic Solvents Used for Nonmetal Emission Measurements

Element	Solvent
C	Decane
F	Fluorobenzene
P	Triethyl Phosphate
Br	Bromobenzene
Cl	Carbon Tetrachloride
I	diiodomethane
S	Carbon Disulfide

mL rather than 10 mL. With tap A open and taps B and C closed, the plasma was ignited by insertion of a tungsten wire into the discharge tube. After ignition of the plasma, tap A was closed and taps B and C were opened to purge the 25 mL conical flask with the helium gas plus the organic nonmetal vapor of interest. The system was allowed to equilibrate for approximately 5 minutes prior to data collection.

Carbon Transitions Observed in the He-HEMIP

Table 11 is a listing of the atomic carbon transitions observed in the spectral region 190 - 500 nm. Energy levels and wavelengths were obtained from Reference 55 and transitions was from References 56-58.

The most intense MIP excited C(I) line that was observed occurred at 247.86 nm. A wavelength scan of the two most intense lines observed which included the 247.86 nm atom line is shown in Figure 19.

Fluorine Transitions Observed in the He-HEMIP

Table 12 summarizes the prominent fluorine emission lines observed, along with upper state energies for the wavelength region studied. The energies and wavelengths were obtained from Reference 40. Figures 20 and 21 indicate the origins of the more important lines listed in Table 12 [56,59]. A number of known transitions originating from

TABLE 11: Carbon Lines Observed in the He-HEMIP

Wavelength (nm)	Transition[a]	Energy (cm^{-1})[b]
247.86	$2p^2 {}^1S_o - 3s {}^1P^o$	21,648-61,982
193.09	$2p^2 {}^1D_2 - 3s {}^1P^o_1$	10,194-61,982

[a] References 56-58.

[b] Reference 55.

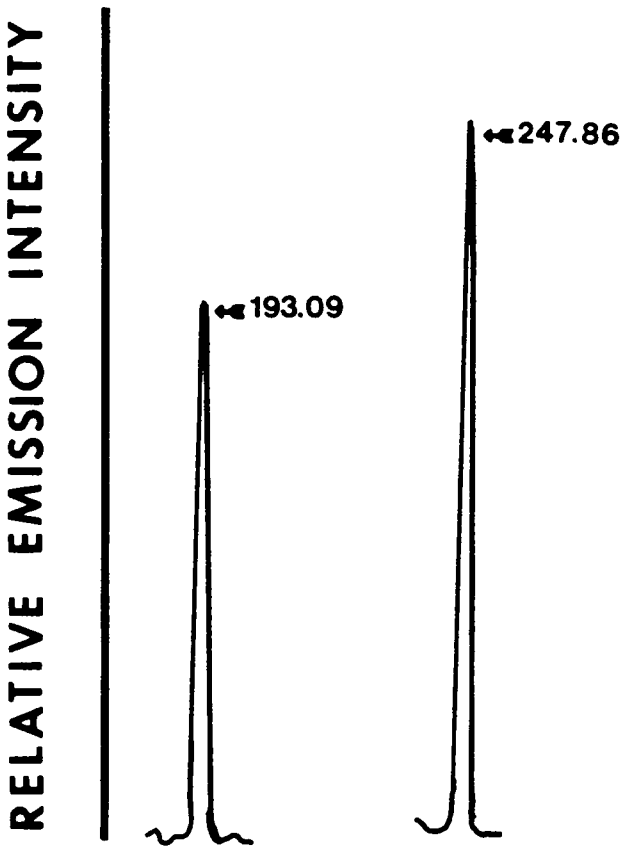

FIGURE 19: Wavelength scans for carbon emission in the He-HEMIP.

Table 12: Most Intense Fluorine Emission Lines Observed in the He-HEMIP

λ (nm)	Transition[a]	Energy (cm^{-1})[b]
623.964	$3s^4P_{5/2}$-$3p^4S^o_{3/2}$	102,407-118,429
634.85	$3s^4P_{3/2}$-$3p^4S^o_{3/2}$	102,681-118,429
641.37	$3s^4P_{1/2}$-$3p^4S^o_{3/2}$	102,841-118,429
677.40	$3s^4P_{5/2}$-$3p^4D^o_{3/2}$	102,407-117,165
683.43	$3s^4P_{3/2}$-$3p^4D^o_{3/2}$	102,681-117,309
685.60	$3s^4P_{5/2}$-$3p^4D^o_{7/2}$	102,407-116,988
687.00	$3s^4P_{1/2}$-$3p^4D^o_{1/2}$	102,841-117,393
690.25	$3s^4P_{3/2}$-$3p^4D^o_{5/2}$	102,681-117,165
690.98	$3s^4P_{1/2}$-$3p^4D^o_{3/2}$	102,841-117,309
703.75	$3s^2P_{3/2}$-$3p^2P^o_{3/2}$	104,732-118,938
712.80	$3s^2P_{1/2}$-$3p^2P^o_{3/2}$	105,057-119,083
720.24	$3s^2P_{1/2}$-$3p^2P^o_{3/2}$	105,057-118,938
731.10	$3s^2P_{3/2}$-$3p^2S^o_{1/2}$	104,732-118,406
733.20	$3s^4P_{5/2}$-$3p^4P^o_{3/2}$	102,407-116,042
739.87	$3s^4P_{5/2}$-$3p^4P^o_{5/2}$	102,407-115,919
742.57	$3s^4P_{3/2}$-$3p^4P^o_{1/2}$	102,681-116,144
748.27	$3s^4P_{3/2}$-$3p^4P^o_{3/2}$	102,681-116,042
755.22	$3s^4P_{5/2}$-$3p^4P^o_{5/2}$	102,681-115,919
757.34	$3s^4P_{3/2}$-$3p^4P^o_{3/2}$	102,841-116,042
775.47	$3s^2P_{3/2}$-$3p^2D^o_{5/2}$	104,732-117,624

[a,b] Reference 40.

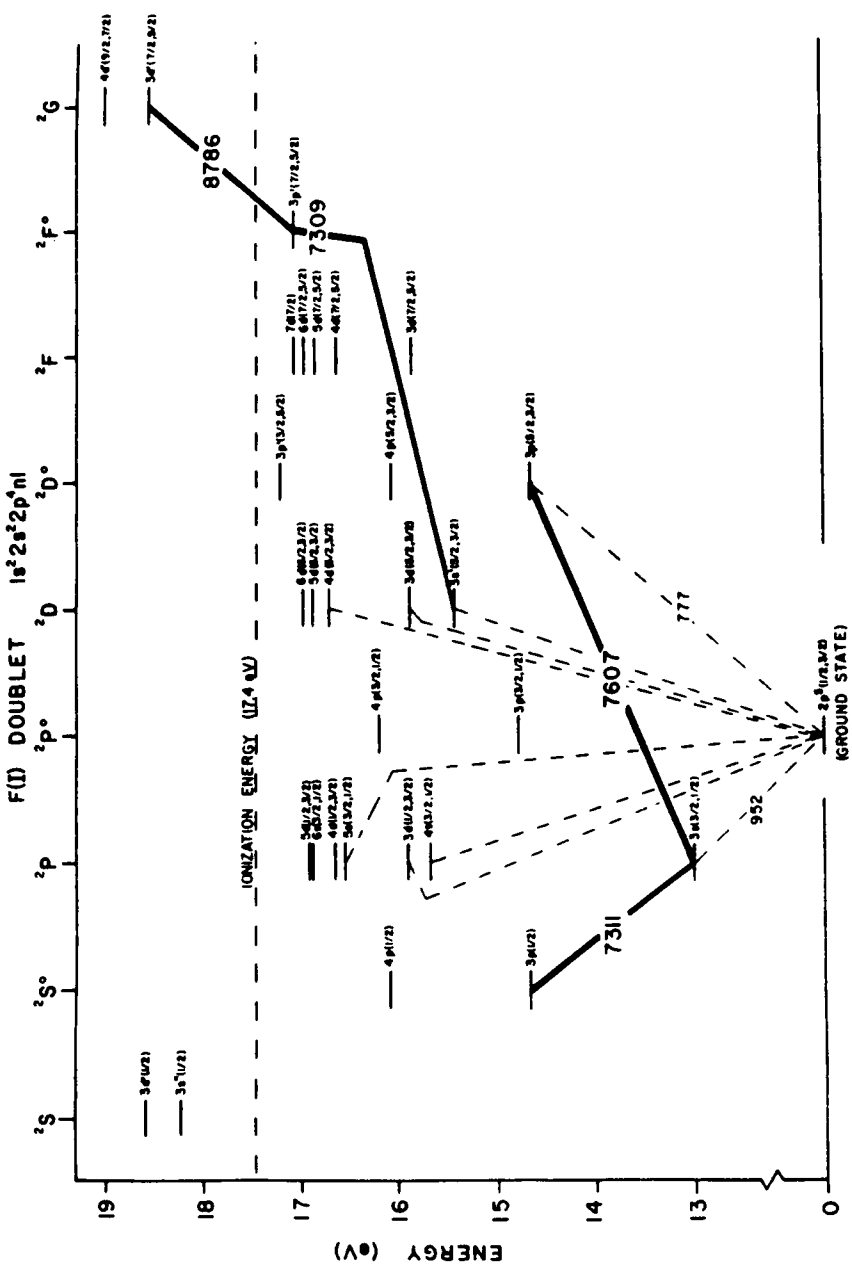

FIGURE 20: Partial Grotrian diagram of the doublet atomic fluorine transitions (From Ref. 59).

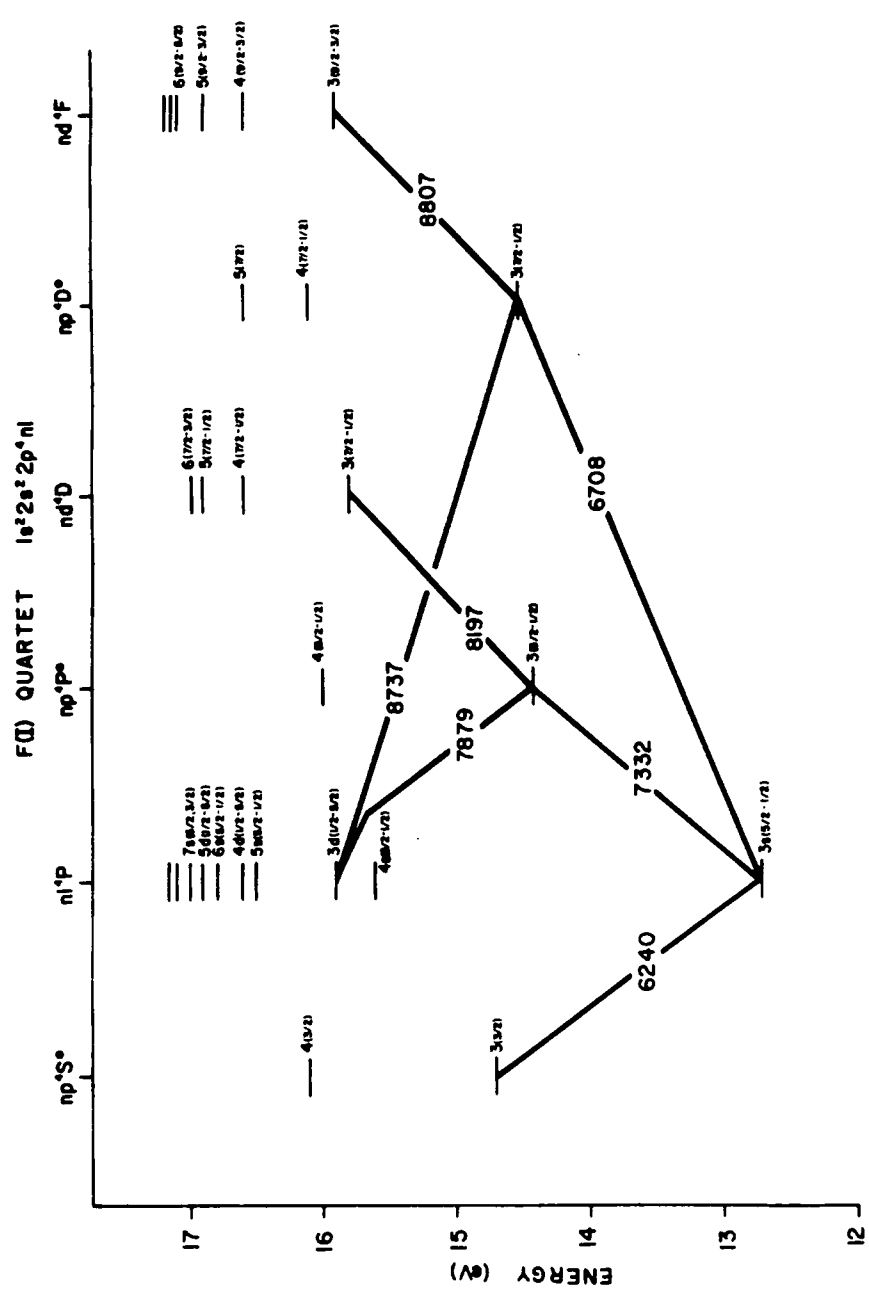

FIGURE 21: Partial Grotrian diagram of the Quartet fluorine transitions (From Ref. 59).

term multiplicities >1 produced a group of fluorine emission lines close in wavelength (i.e., 677.39, 679.55, 683.42, 685.56 (the strongest line), 687.02, 690.24, and 690.98).

Most of the major transitions with upper states greater than or equal to 18.5 were observed as predicted from atomic diagrams. Grotrian diagrams indicate that no F(I) lines can occur between 100 nm and 350 nm [59].

The most intense F(I) line observed in this study is the 685.6 nm line which originates from the $3s^4P_{(5/2)}$ $-3P^4D^0_{(7/2)}$ transition.

The principle reasons for loss of signal response at long wavelengths are the decrease in resolution of the grating of the 0.35m monochromator and the decrease in the signal response of the photomultiplier tube. Therefore, further studies in the near-IR region were abandoned.

Chlorine, Bromine, Phosphorus, and Iodine Observed Transitions in the He-HEMIP

The most intense chlorine, phosphorus, iodine, and bromine atomic emission lines in the spectral region 200-800 nm along with their transitions are listed in Table 13. An abbreviated scan of the region for chlorine is shown in Figure 22.

The most intense Cl(I), Br(I), I(I), and P(I) line observed was at 479.45 nm, 470.49 nm, and 206.23 nm, 213.54 respectively. These lines originated from the

Table 13: Most Intense Cl, P, I and Br Emission Lines Observed in the He-HEMIP

λ(nm)	Transition[a]	Energy (cm^{-1})[b]
	Chlorine	
479.45	$4s^5S^o_2$-$4p^5P_3$	107,879-128,703
481.01	$4s^5S^o_2$-$4p^5P_2$	107,879-128,663
481.95	$4s^5S^o_2$-$4p^5P_1$	107,879-128,662
	Phosphorus	
213.55	$3p^3\ ^2D^o_{3/2}$-$4s^2P_{3/2}$	11,362-58,174
214.91	$3p^3\ ^2D^o_{3/2}$-$4s^2P_{1/2}$	11,362-57,877
	Iodine	
206.24	$5p^5\ ^2P^o_{1/2}$-$6s^2P_{3/2}$	7,603-56,093
	Bromine	
470.49	$5s^5S^o_2$-$5p^5P_3$	93,927-115,176
478.55	$5s^5S^o_2$-$5p^5P_2$	93,927-114.818
481.67	$5s^5S^o_2$-$5p^5P_1$	93,927-114,683

[a] References 56-58.

[b] Reference 55.

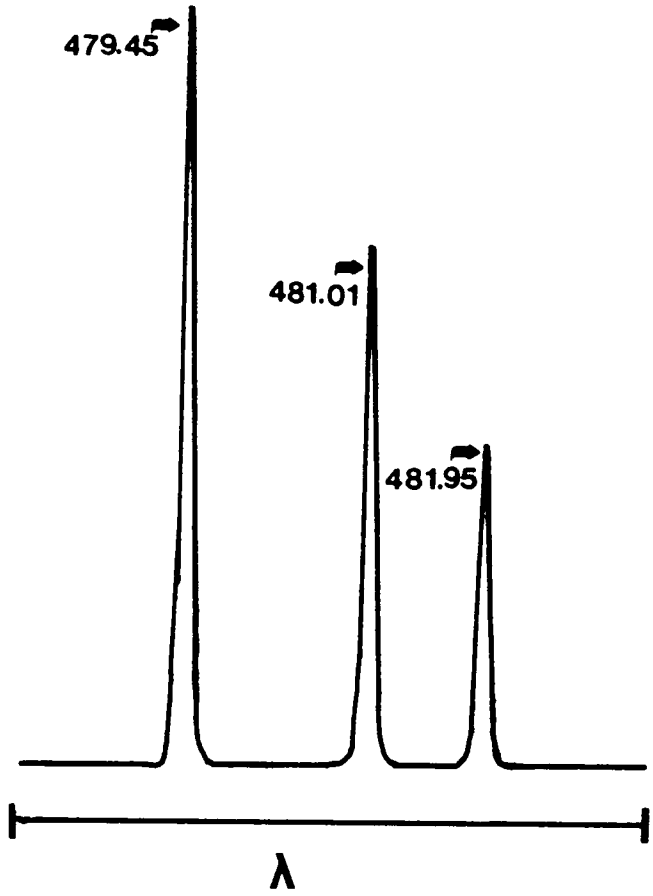

FIGURE 22: Abbreviated wavelength scan of chlorine emission in the He-HEMIP.

$4s^5S^0_{(2)}$-$4p^5P_3$ transition for Cl(I); the $5s^5S^0_{(2)}$-$5p^5P_3$ transition for Br(I); the $5p^5$ $^2p^0_{(1/2)}$-$6s^2P_{(1/2)}$ transition for I(I); and the $3p^3$ $2D_0^{(3/2)}$-$4s\ ^2P_{(3/2)}$ transition for P(I).

Sulfur Observed Transitions

Sulfur scans were obtained with and without a purge system, as described in Chapter 2. Table 14 lists the atomic lines observed from 170-500 nm.

The most sensitive MIP excited atomic sulfur emission line was observed at 180.7 nm (argon purged environment). The 217.1 nm line also proved to be sensitive when compared to other sulfur lines observed in a non-purged environment. Because of the complexity of the argon purged system, the 217.1 nm line may be of particular importance for the determination of sulfur via direct nebulization.

Determination of Aqueous Nonmetals by Direct Nebulization

Nonmetal detection limits for aqueous samples are listed in Table 15, and the results of the He-HEMIP values are compared to data from Michlewicz and Carnahan using a 21 L/min He MIP and an applied power of 500 W. In addition, a MAK pneumatic nebulizer was employed by Michlewicz and Carnahan. In terms of droplet size distributions, the MAK produces a much smaller droplet size distribution than does the Meinhard nebulizer used in this work [61,62]. Because

TABLE 14: Sulfur Emission Lines Observed in the He-HEMIP

	Wavelength (nm)
S (I)	180.73
S (I)	182.04
S (I)	182.63
S (I)	190.03
S (I)	191.47
S (I)	216.89
S (II)	481.55
S (II)	492.41
S (II)	545.39
S (II)	560.61
S (II)	563.99

droplet sizes affect the desolvation and vaporization times of the analyte, and the solvent loading, smaller droplets sizes should result in decreased detection limits. In the case of the He-HEMIP, the detection limits are significantly lower than that reported for the high power MIP Carnahan cavity and MAK nebulizer. With the desolvation apparatus shown in Figure 7, the detection limit for chlorine using the He-HEMIP was determined to be 30 ppb.

Also reported in Table 15 are detection limits for S and P using the He-HEMIP. These detection limit values for S and P are the first reported for helium MIP-AES with the use of direct nebulization without desolvation and a Beenakker modified cavity.

Determination of Nonmetals in NBS Simulated Rain Water

The ability of the MIP to selectively and accurately determine nonmetals in complex aqueous samples is shown in Table 16. Values in the parentheses represent standard deviations.

It should be noted that the chloride detection values provided by NBS were not certified.

CONCLUSIONS

It has been established that the simple and inexpensive atmospheric He-HEMIP system described can be used for

TABLE 15: He-HEMIP Nonmetal Limits of Detection in ppm (k=2)

Element	λ (nm)	LOD	LOD[a]
Br	478.5	2	60
I	206.2	1	7
P	213.6	0.4	-
S	217.1	1.2	-
Cl	479.5	0.8 (0.03)[b]	2

[a] Reference 40.

[b] Desolvation system used.

TABLE 16: Values for the Determination of Nonmetals in NBS 2694 Simulated Rain Water

Element	Accepted Value 2694-I	Measured Value 2694-I	Accepted Value 2694-II	Measured Value 2694-II
F	0.054(0.002)[a]	0.061(0.001)	0.098(0.007)[a]	0.127(0.003)
Cl	0.24[b]	0.19(0.02)	1.0[b]	0.84(0.05)
S	2.75(0.05)[c]	2.78(0.08)	10.9(0.2)[c]	10.7(0.1)

[a] Ion Chromatography, Conductimetry

[b] Ion Chromatography, Conductimetry

[c] Ion Chromatography, Isotope Dilution Thermal Ionization Mass Spectrometry

qualitative and quantitative determinations of halogens with high selectivity and sensitivity. This technique shows great promise for the direct determination of nonmetals in aqueous and organic solutions. All of the emission lines used in this study arose from nonresonant transitions and should be reasonably immune to self-absorption.

CHAPTER 6

DETERMINATION OF SULFUR IN COALS by MIP-AES

A primary concern of all developed countries is the control and monitoring of environmental pollutants. In particular, there is a need for analytical methods for the determination of minor and total concentrations of sulfur, released as SO_2 into the atmosphere, from the combustion of fuels. SO_2 is a major cause of combustion equipment corrosion and is a precursor for the formation of acid rain.

The determination of sulfur in coal is, by definition, part of the ultimate analysis of coal [62]. Sulfur analysis results obtained are used to serve several objectives: the evaluation of coal preparation methods; the evaluation of the potential sulfur emissions from coal combustion or conversion processes; and the evaluation of coal quality in relation to contract specifications; as well as other commercial or scientific interests.

Traditionally, the sulfur in coal has been divided into two classes [63]: inorganic sulfur and organic sulfur. In the class of inorganic sulfur, two types of compounds are considered: the disulfides and the sulfates. Organic sulfur is all the sulfur which is connected to the hydrocarbon matrix. The working definition of the classes of sulfur is as follows [63-66]:

(1) The sulfate sulfur is the sulfur equivalent of the amount of sulfate ion which dissolves in 2:3 HCl in 30 min.

(2) The pyritic sulfur is the sulfur equivalent of the iron which dissolves in boiling 2N HNO_3 in 30 min.

(3) The organic sulfur is the difference between the total sulfur and the sum of the sulfatic and pyritic sulfur.

The total sulfur in coal varies in concentration range of 0.2-11 wt. % [67]. Most of the sulfur is in the form of FeS_2. The amount of organic sulfur is usually one-half to one-third of the total concentration of sulfur. The amount of sulfate sulfur rarely exceeds 0.1 wt. %.

Iron disulfide, FeS_2 appears in two crystalline forms, the pyrite (cubic) and the marcasite (rhombic) [68]. Most of the FeS_2 is pyritic, so the term "pyrites" is often used to designate all FeS_2. The chemical reactivity of the two forms are similar, and they are rarely considered separately. However, the origin of the pyrite and marcasite may be different. The accepted theory is that FeS_2 appears in the form of loose crystals which form vine-like structures within organic seams [68-70].

The sulfate sulfur appears mainly in the form of calcium and iron sulfates [63.68,69], and appears in the form of loose crystals. All of the organic sulfur is

believed to be divalent. Organic sulfur is spread throughout the organic matrix [68,70,71].

The interactions of sulfur in coal pyrolysis can be divided into four subsystems, which interact with each other as shown in Figure 23 [63].

(1) The iron pyrites which decompose thermally and interact with the gas phase.

(2) The organic material which decomposes. The products of the reactions in the condensed organic phase are determined by the chemical reaction, but are strongly affected by the local mass transfer conditions, and by temperature. The products of this subsystem will be affected by the particle size and the heating rate of the coal sample.

(3) The mineral matter: CaO, MgO, FeO, SiO_2, and Al_2O_3.

(4) Reactions in the gas phase, between the components that escaped from the condensed phases. The products of this subsystem will be a strong function of the pyrolysis chamber and the operational conditions. The gas in the subsystem also transfers sulfur from the chamber to the surroundings.

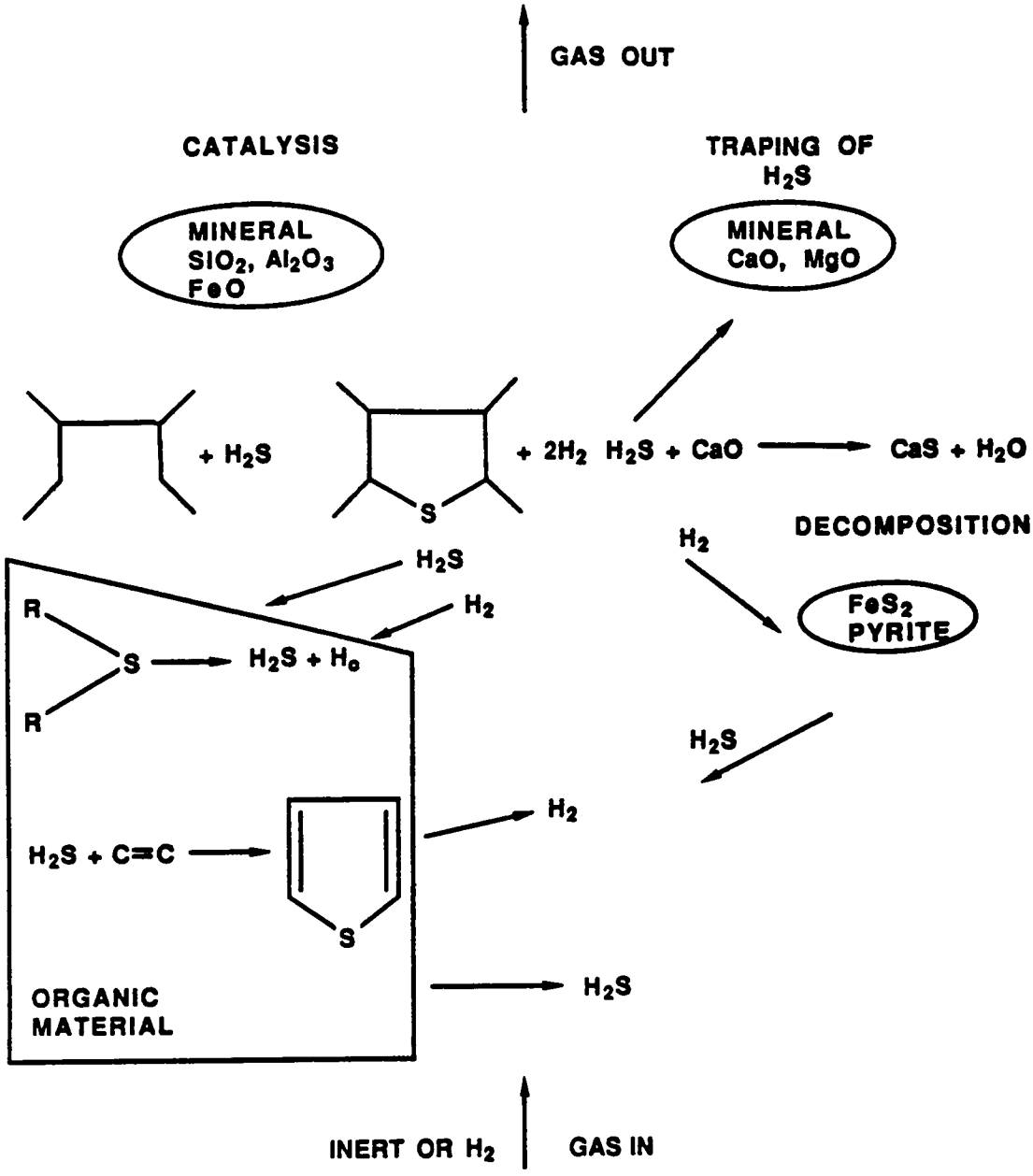

FIGURE 23: Reaction of sulfur compounds in coal pyrolysis chamber (From Ref. 63).

Subsystem 1: The most important variables that will control the reactions in this subsystem are:

(1) The rate of decomposition of FeS_2 crystals, which is controlled by temperature.

(2) The composition of the gaseous environment in the pyrolysis chamber, which controls the rate of sulfur transport from the surface.

The desulfurization of FeS_2 in coal is thought to be complete at temperatures above 700°C [72].

Subsystem 2: The most important variables that will affect the sulfur products of the reactions in the condensed phase are [63]:

(1) The volatility of the coal. Larger fractions of organic sulfur are volatilized from high volatile coal.

(2) The initial distribution of the sulfur groups in the organic matrix, namely, how much organic sulfur is present, and in what forms. Sulfur in the forms of organic sulfides, disulfides, and thiols may decompose and form H_2S. Thiophenic groups are stable and will not decompose at temperatures up to 500-800°C or more. Moreover,

some of the organic sulfides may go dehydrocyclation and stabilize as thiophenes.

(3) The coal composition. If the coal contains many reactive groups like double bonds, kenotic or quinonic groups, hydroxyls etc., they may react with H_2S and tie it to the organic matrix as stable organic sulfur.

(4) The temperature and the rate of heating, which controls the relative rates of each reaction type at any instance. Since the rates of formation of active groups, i.e., double bonds, are also a function of the temperature, and will affect the sulfur distribution by increasing the rates of the reactions of the sulfur components, and by creating or consuming groups that react with H_2S.

(5) The dimensions of the coal particles, which will control the distance that each molecule of H_2S will have to diffuse before it reaches the surface of the coal.

It should be noted that coal is not an isotropic material, and the rates of diffusion of gases are different in each direction. However, a larger fraction of the sulfur pool can be volatilized when the same coal is crushed to produce smaller particles [73].

Subsystem 3: The most important variables which control the reactions in this subsystem are [63]:

(1) The amount and form of the basic materials: the Ca, Mg, and Fe salts.
(2) The temperature.
(3) The hydrogen and hydrogen sulfide particle pressure in the pyrolysis chamber.
(4) The amount of acidic minerals and their composition.
(5) The flow pattern and the residence time of the gas in the chamber.

H_2S that is released from the organic sulfides (below 400-450^{o}C) and from pyrite hydro- desulfurization, (released in the range of 550-700^{o}C) will rapidly sulfidize the basic minerals. Desulfidation of calcium sulfide will not occur in practice. Desulfidation of FeS becomes important about 950^{o}C when high hydrogen partial pressures and low H_2S partial pressures are applied.

The catalytic activity of the acidic mineral matter will be observed at temperatures above 350-600^{o}C. The main effect is catalytic decomposition of the mercaptans and the aliphatic and aromatic sulfides. The catalytic activity will depend on the partial pressures of H_2 and H_2S, on the

temperature, on the pressure, and on the flow pattern in the chamber.

Subsystem 4: The gas phase is the media through which the coal communicates with the outside and the organic material communicates with the condensed phases, or can leave the chamber unchanged.

The most important variables which control the behavior of the gas phase are [63]:

(1) The flow pattern of the chamber, which determines the residence time of the gas in the chamber.
(2) The temperature, which determines the rates in the gas phase reaction.
(3) The surface conditions of the organic and inorganic condensed phase, which determine the rates of the gas-solid or gas-liquid reactions, including catalysis of the gas phase reactions on the surface of silicates or FeS crystals [73]. For temperatures above 750^{o}C, thermodynamics will determine the composition.

In this chapter a new method for sulfur monitoring has been developed based on MIP-AES. This method involves the use of the helium high efficiency MIP (He-HEMIP) as an atomization source for the determination of sulfur during coal pyrolysis. Three different methods are evaluated. The

first method involves a leaching technique for the determination of sulfate sulfur; the second method uses H_2O_2 as a trap for the collection of sulfur gases during pyrolysis; and the third method involves on-line analysis of sulfur gases during the coal pyrolysis process.

EXPERIMENTAL

All MIP operation conditions were the same as outlined in Chapter 2. The monochromator and optical path were purged with argon one hour prior to all experiments.

Four types of coal samples were obtained for this study, specifically R-Coal, Buller Coal, Leco coal Standard 501-020 (Leco Corporation, St. Joseph, MI), and Leco coke Standard 767-759 (Leco Corporation, St. Joseph, MI).

Two procedures were used: one for the determination of soluble sulfates, the other to the determine the total concentration of sulfur in the coal samples. Procedure 1 involved a modification of the leaching technique employed by Caroli et al plus a variation of the ASTM Standard Methods Procedure D4239 [74,75]. In this revised procedure, a known weight of a coal sample was introduced into a 500-mL round bottom flask with the addition of 200 mL of 0.6 % HCL and 1 mL of 30 % m/V H_2O_2. Six drops of ethanol was added to facilitate the wetting process. After mixing, the mixture was digested for 20 minutes and filtered using No.

10 filter paper. Care was taken to transfer all of the material by repeated washings with hot deionized water. The standard for calibration curves, Na_2SO_4, was similarly treated. A flow diagram is shown in Figure 24.

The second procedure (off-line method) is illustrated in Figure 25, was used for the total determination of sulfur by pyrolysis. Two separate experiments were conducted. In the first experiment, the coal sample was weighed and covered in a 50% mixture of Al_2O_3 and V_2O_5 to facilitate combustion. The samples were then placed in a tube furnace (Lindberg Corp.) at 1200°C and purged with 2 mL/min O_2 for one and one-half hours. The gases evolved were collected in a 250 mL volumetric flask containing 100 mL of H_2O_2.

The second experiment for procedure 2 (on-line method) was also used for the determination of total sulfur by pyrolysis using the same procedure as the off-line method; the exception was that instead of the sulfur gases being introduced into the flask, they were introduced directly into the center tube of the MIP torch for analysis (see Figure 26). An additional flow of 2 mL/min of He was added to the 2 mL/min O_2 flow into the pyrolysis for ease of plasma operation. The gas transfer line was maintained at a temperature of 200°C to prevent loss of sulfur by condensation.

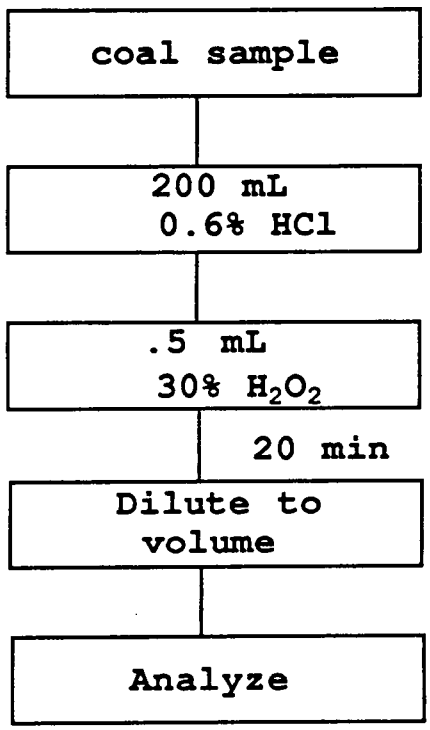

FIGURE 24: Flow diagram for the determination of soluble sulfate in coal.

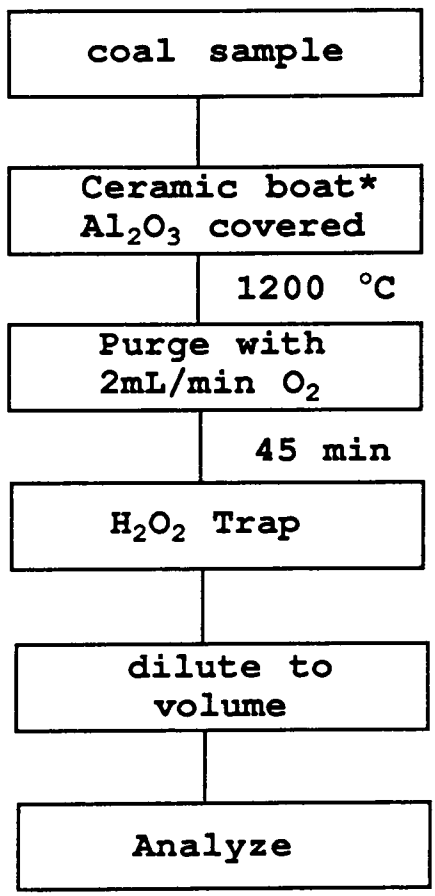

***carbon and sulfur free**

FIGURE 25: Diagram for the determination of total sulfur by the high temperature tube furnace combustion method (off-line).

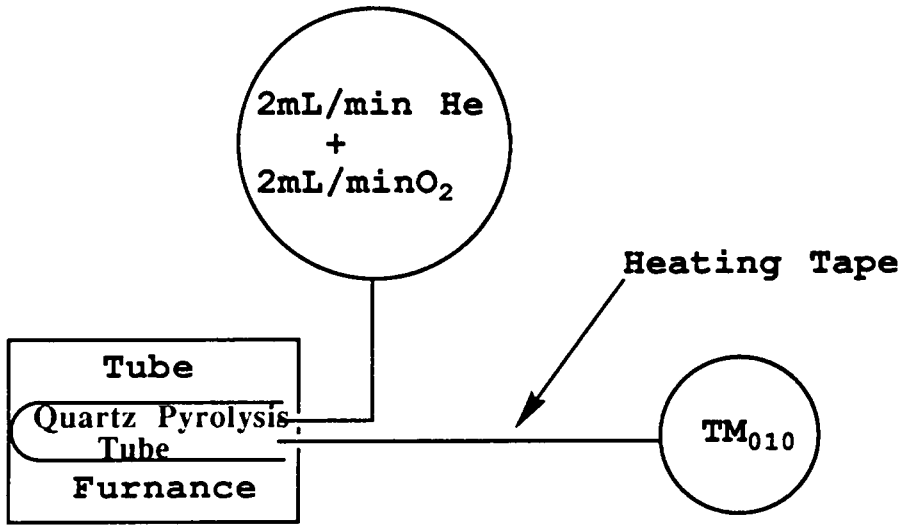

FIGURE 26: Diagram for the determination of total sulfur by the high temperature tube furnace combustion method (on-line).

RESULTS AND DISCUSSION

Effect of the Chemical Composition of Coal: Matrix Effects

Since coal exists naturally in several forms (pyritic and organic), concern existed as to whether the chemical form of sulfur (matrix) played an important role on the emission signal. The emission intensity of sulfur at 180.7 nm was determined for four 1000 ppm solutions of sulfur. The four compounds studied are as follows: ammonium sulfate, sodium sulfate, sulfuric acid, and thiourea. The samples ranged from inorganic (ammonium sulfate, sodium sulfate, and sulfuric acid) to organic (thiourea). The results of the relative intensity study are shown in Table 17. Statistically there appeared to be no difference in the emission intensity based on the form of sulfur introduced into the He-HEMIP. Therefore, the He-HEMIP seems to be immune to interferences from carbon containing compounds, as well as those from easily ionizable elements (see chapter 4). For all work, sodium sulfate and sulfuric acid were used as standards for calibration curves. Matrix matching or standard addition techniques were not attempted.

Linearity

Linearites are shown in Figure 27. Concentrations above 1000 ppm were not attempted because of the low concentrations of sulfur that exist naturally in coals.

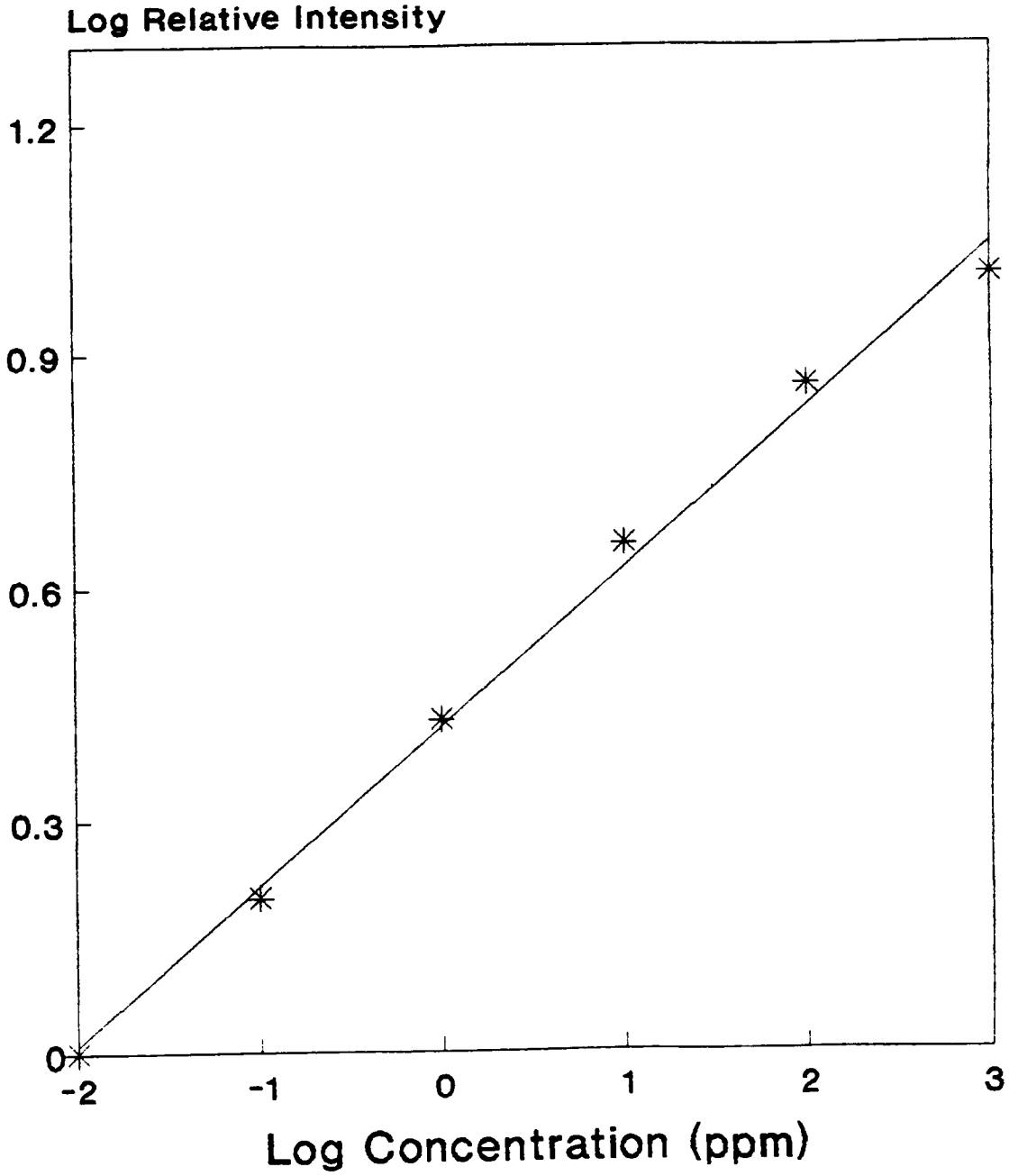

FIGURE 27: Sulfur calibration curve.

TABLE 17: Emission Signals at 180.7 nm using Various Standards (1000 ppm) for Sulfur

Standard	Emission Signal
Ammonium Sulfate	100
Sodium Sulfate	100.6
Sulfuric Acid	99.7
Thiourea	99.8

Generally, greater than 4 orders of linear dynamic range was obtainable.

Sulfur Measurements

Table 18 summarizes values obtained for the determination of soluble sulfates in the four coal samples studied. No information for comparison was available. However, from the measurements presented below, there is evidence that the values are satisfactory.

Results of the off-line total sulfur procedure are shown in Table 19. It is apparent from these results that the He-HEMIP is capable of quantifying low concentrations of sulfur in complex matrices. The value for R-Coal is believed to be lower and more accurate than that reported by the DCP method of slurry analysis, based on the statistical accuracy of the remaining coal samples using the He-HEMIP. This discrepancy may be explained by the fact that aqueous samples are more efficiently atomized in an atomization source than those nebulized as slurries.

The on-line method of sulfur sample introduction was conducted using Leco standard 501-020. As can be seen from Figure 28 the sulfur signal was detected and quantified. The Leco standard 501-020 contains 2.86 wt. % as determined by the Leco SC-132 Infrared Sulfur Determinator and was verified by the off-line determination by MIP-AES. Interestingly, analysis by MIP-AES of the standard using

TABLE 18: Values for the Determination of Soluble Sulfur in Coals

Coal Sample	Accepted value, %	Measured[+] value, %
R-coal	N/A*	0.45(0.01)
Bueller	N/A*	0.39(0.01)
Leco Standard 501-020	N/A*	0.98(0.02)
Leco Standard 767-759	N/A*	0.06(0.01)

+ Na_2SO_4 used for calibration curve

* Data not available

TABLE 19: Values for the Determination of Total Sulfur in Coal Using the Off-Line Method

Coal Sample	Accepted value, %	Measured value, %
R-coal	1.60 +	1.44(0.02)
Bueller	1.63(0.01)*	1.69(0.02)
Leco Standard 501-020	2.86(0.06)*	2.84(0.03)
Leco Standard 767-759	0.79(0.03)*	0.76(0.02)

+ DCP slurry method

* Leco SC-132 Infrared Sulfur Determinator

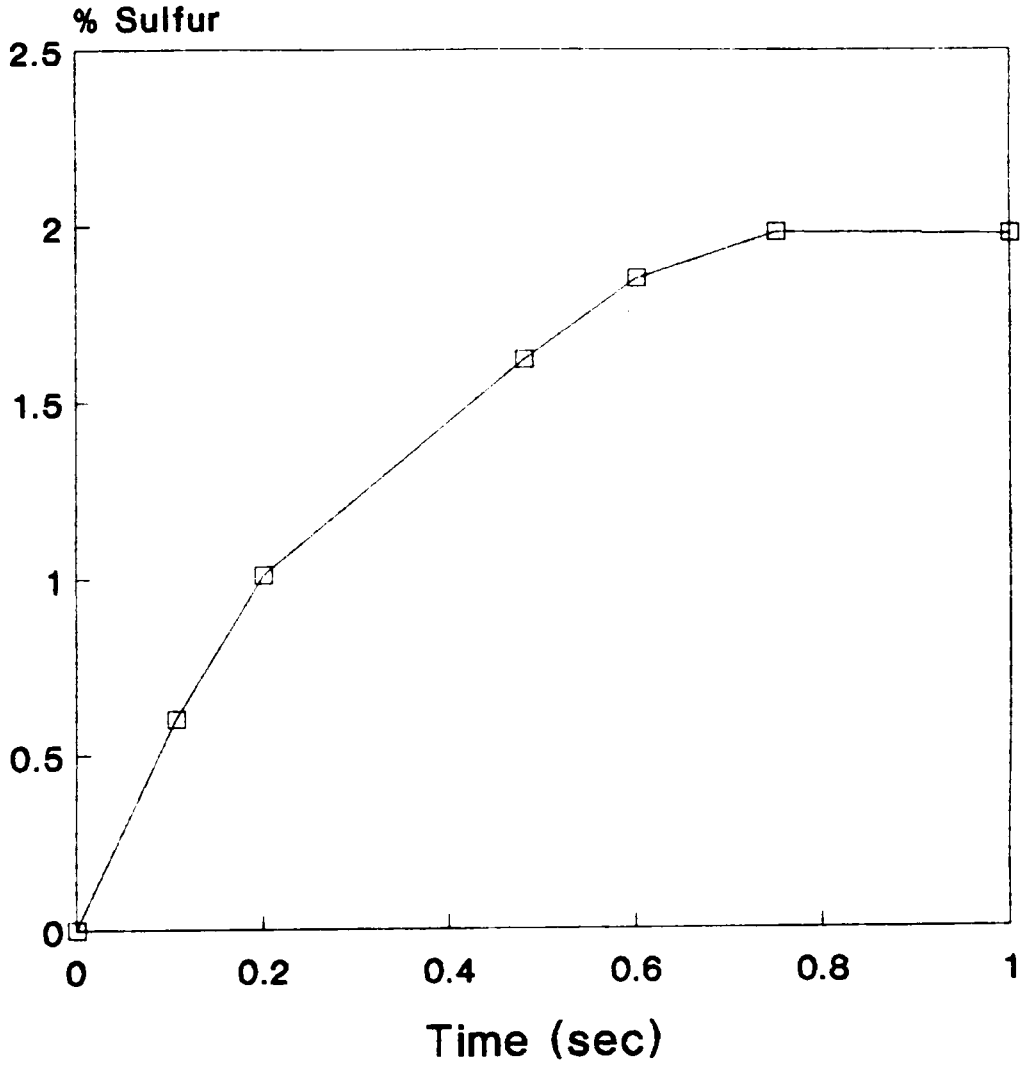

FIGURE 28: Plot of percent sulfur vs. time in the pyrolysis chamber using the on-line method.

aqueous samples for the calibration curve shows that the total concentration of S in the Leco standard to be approximately 1.9 wt. %. This discrepancy in wt. % was investigated and found to be from condensation of sulfur on the pyrolysis transfer tube and possibly on the calibration methods used. The pyrolysis transfer tube length was approximately, 21.5 in long. Apparently, this distance is too long for the sulfur containing compounds to travel without condensation at the temperature of 200^{o}C.

Conclusion

Evaluation of the He-HEMIP as a routine detector for sulfur in coal has been presented. Clear evidence have been shown that the MIP is capable of desolvating, atomizing, and exciting complex samples without the aid of desolvation. As per the analysis of sulfur in coal samples via leaching or digestion the MIP clearly has taken its place for these analysis. However, additional work is needed for calibration procedures using the on-line method for sulfur determination. Finally, most of the condensation can be decreased by increasing the temperature of the pyrolysis transfer tube and decreasing its length.

CHAPTER 7

CONCLUSIONS

The primary thrust of this dissertation is the development of a new helium sensitive and selective excitation source using the high efficiency microwave induced plasma (He-HEMIP). The He-HEMIP provides a significant low power advantage when compared to other helium microwave plasmas. It is self-igniting and easily tuned. It operates at a low gas consumption rate (1 L/min) and facilitates the introduction of aqueous liquid samples. The cost of the system is low, the most expensive component of the system is the generator. However, due to the increased consumer market for microwave ovens the microwave sources, magnitrons are constantly decreasing in cost.

The He-HEMIP has fulfilled a set of ideal requirements for elemental analysis are presented in this dissertation: the plasma possesses high excitation and thermal temperatures which permit efficient desolvation, vaporization, atomization, and excitation of liquid and gaseous samples. Interelement interferences are minimal using AES and non-existence with AFS. The system provides for rapid analyses. The precision and accuracy of the He-HEMIP are acceptable for trace and ultra-trace analysis. It is applicable to the analysis of liquids and gaseous

samples with minimal preliminary sample preparation or manipulation. The He-HEMIP provides ppb detection limits and large linear working ranges, up to five and one-half orders.

More specifically, the He-HEMIP approaches local thermodynamic equilibrium (LTE). Evidence in this work is based on the fact that the excitation temperature is approximately equal (within statistical error) to the ionization temperature. Unfortunately, without the knowledge of the plasma gas temperature and electron temperature, the existence of LTE cannot be conclusively confirmed or rejected.

The He-HEMIP was evaluated in this dissertation as an atomization source for the determination of metals using atomic emission spectrometry (AES) and atomic fluorescence spectrometry (AFS) with direct aqueous nebulization. All studies were conducted with the plasma in the radial position. The He-HEMIP functions better as an atomization source for AFS than for AES. In contrast to AES, AFS requires that the plasma only vaporize and dissociate the analyte. The excitation process occurs through the use of the source radiation, hollow cathode lamps. With AES, detection limits for metals were determined to be in the low to sub-ppb range and were found not statistically different from those reported for HCL-ICP-AFS. Linear ranges for AES

and AFS ranged from four up to five and one-half orders of concentrative magnitude. Ionization interferences are minimal, and phosphate interferences were not found to occur.

The He-HEMIP is also a sensitive and selective detector for nonmetals in aqueous solution, as reported in this work. Detection limits for Br, I, P, S, Cl are 2, 1, 0.4, 1.2 and 0.8 using direct aqueous nebulization without prior desolvation. With desolvation the detection limit for Cl was further lowered to 0.03 ppm. These detection limit values are the lowest reported todate using a plasma source. The detection limit values for S and P are the first reported for MIP-AES with the use of direct nebulization and a Beenakker type cavity. The precision and accuracy of the He-HEMIP was verified using NBS simulated rain water. Detection values of the He-HEMIP compared favorably with the NBS standards.

A new method of sulfur monitoring was also developed in this study. This method was based on the use of the He-HEMIP as an atomization source for the determination of sulfate sulfur and sulfur during pyrolysis (on-line and off-line). Detection values using the He-HEMIP method were consistent with those of certified standards.

The work that is represented in this dissertation provides a detailed investigation of the characteristics of

a new plasma source, the He-HEMIP. The high sensitivity of the He-HEMIP makes it a potentially powerful tool for metals and nonmetals.

REFERENCES

1. R. H. Wendt and V. A. Fassel, Anal Chem., 37, 920(1965).

2. S. Greenfield, H. McD. McGreachin, and P. B. Smith, Talanta, 23, 1(1976).

3. R. M. Barnes, CRC Crit. Rev. Anal. Chem., 203(1978).

4. V. A. Fassel, Anal. Chem., 51, 1290A(1979).

5. V. A. Fassel, Science, 202, 183(1978).

6. R. M. Barnes, Phil. Trans. R. Soc. Lond., A305, 499(1982).

7. J. P. Matousek, B. J. Orr, and M. Selby, Prog. Analyt. Atom. Spectrosc., 7, 275 (1984).

8. A. T. Zander and G. M. Hieftje, Appl. Spectrosc., 35, 357(1981).

9. J. W. Carnahan, Am. Lab., 13(8), 36(1983).

10. R. F. Browner and A. W. Boorn, Anal. Chem., 56, 786A(1983).

11. R. F. Browner and A. W. Boorn, Anal. Chem., 56, 875A(1984).

12. M. Selby and G. M. Hieftje, Pittsburg Conference, 1985, Abstract 1019.

13. C. I. M. Beenakker, B. Bosman, and F. W. J. M. Boumans, Spectrochim. Acta, 34B, 373(1978).

14. D. L. Hass and J. A. Caruso, Anal. Chem., 47, 194(1984).

15. K. C. Ng and W. L. Shen, Anal. Chem., 58, 2084(1986).

16. C. I. M. Beenakker, Spectrochim. Acta, 31B, 483(1976).

17. J. E. Freeman and G. M. Hieftje, Spectrochim. Acta, 40B, 653(1985).

18. C. F. Bauer and R. K. Skogerboe, Spectrochim. Acta, 38B, 1125(1983)

19. B. W. Smith and M. L. Parsons, J. Chem. Ed., 50, 679(1973).

20. L. J. Galante, M. Selby, and G. M. Hieftje, Appl. Spectrosc., 42, 559(1988).

21. L. G. Matus, C. B. Boss, and A. N. Riddle, Rev. Sci. Instrum., 54, 1667(1983).

22. B. Burns and C. B. Boss, North Carolina State University, unpublished work.

23. R. D. Deutsch and G. M. Hieftje, Appl. Spectrosc., 39, 214(1985).

24. "Nomenclature, Symbols, Units, and their Usage in Spectrochemical Analysis II," Spectrochim. Acta., 33B, 242(1978).

25. "Guidelines for Data Aquisition and Data Quality Evaluation in Environmental Chemistry," Anal. Chem., 52, 713A(1983).

26. G. L. Long and J. D. Winefordner, Anal. Chem., 55, 713A(1983).

27. P. W. J. M. Boumans, "Theory of Spectrochemical Excitation," Hilger and Watts, London (1966).

28. D. J. Kalnickly, V. A. Fassel, and R. N. Knisely, Appl. Spectrosc., 31, 137(1977).

29. M. W. Blades, B. L. Caughlin, Z. H. Walker and L. L. Burton, Prog. Analyt. Spectrosc., 10, 57(1987).

30. H. R. Griem, "Spectral Line Broadening by Plasmas," Academic Press, New York, (1974).

31. M. W. Blades, B. L. Caughlin, Spectrochim. Acta, 40B, 579(1985).

32. M. H. Abdallah and J. M. Mermet, Spectrochim. Acta, 37B, 391(1982).

33. K. Tanabe, H. Haraguchi, and K. Fuwa, Spectrochim Acta, 38B, 49(1983).

34. J. M. Workman, P. G. Browm, D. C. Miller, C. J. Seliskar, and J. A. Caruso, Appl. Spectrosc., 40, 857(1986).

35. J. F. Alder, R. M. Bombelka and G. F. Kirkbright, Spectrochim. Acta, 35B, 163(1980).

36. S. E. Long and R. F. Browner, Spectrochim. Acta, 43B, 1461(1988).

37. P. E. Waters and C. A. Barnardt, Spectrochim. Acta, 43B, 325(1988).

38. L. D. Perkins and G. L. Long, Fourteenth Meeting of the Federation of Analytical Chemist and Spectroscopic Studies, Detroit (1987), Abstract 40.

39. K. W. Michlewicz and J. W. Carnahan, Anal. Chem., 57, 1092(1985).

40. K. W. Michlewicz and J. W. Carnahan, Anal. Chem., 58, 3122(1986).

41. D. Haas, J. W. Carnahan, and J. A. Caruso, Appl. Spectrosc., 37, 82(1983).

42. K. B. Cull and J. W. Carnahan, Appl. Spectrosc., 42, 1061(1988).

43. G. L. Long and L. D. Perkins, Appl. Spectrosc., 41, 980 (1987).

44. L. D. Perkins and G. L. Long, Appl. Spectrosc., 42, 1285(1988).

45. R. K. Skogerboe and G. N. Coleman, Anal. Chem., 48, 611A(1976).

46. J. C. Van Loon, Anal. Chem., 51, 1139A(1979).

47. D. R. Demers, D. A. Busch, and C. D. Allemand, Am. Lab. 42(3), 167(1982).

48. G. D. Christian, "Analytical Chemistry," John Wiley and Sons, New York (1986).

49. D. C. Harris, "Quantitative Chemical Analysis," W. H. Freedman and Company, New York (1982).

50. D. A. Skoog and D. M. West, "Fundamentals of Analytical Chemisty," Saunders, Philadelphia (1982).

51. K. A. Rubinson, "Chemical Analysis," Little, Brown and Company, Boston (1987).

52. "Modern Methods of Analytical Chemistry," The Dow Chemical Company, Midland, MI.

53. D. D. Nygaard, R. G. Schleicher, and D. A. Leighty, Am. Lab., 17(6), 59(1985).

54. N. W. Barnett and G. F. Kirkbright, J. Anal. At. Spectrosc., 1, 337(1986).

55. A. N. Zaidel, V. Prokofer, S. M. Raiskii, V. A. Slavnyi and E. Ya. Shreider, "Tables of Spectral Lines," Plenum, New York (1970).

56. A. R. Striganov and N. S. Sventitakii, "Tables of Neutral and Ionized Atoms," Plenum, New York (1968).

57. W. L. Weise, M. W. Smith and B. M. Glennon, "Atomic Transition Probilities," NSRDS-NBS-4, U. S. Department of Commerce, U. S. Government Printing Office, Washington, D. C., (1966).

58. S. Bashkin and J. O. Stoner, Jr., "Atomic Energy Levels and Grotrian Diagrams," North-Holland, Elseiver Amsterdam, (1978).

59. R. C. Fry, S. J. Northway, R. M. Brown and S. K. Hughes, Anal. Chem., 52, 1716(1980).

60. R. F. Browner, Department of Chemistry, Georgia Tech, personal communication.

61. R. D. D. Olsen and A. Strasheim, Spectrochim. Acta, 38B, 973(1983).

62. "Annual Book of ASTM Methods," Method D3177, Philadelpnia (1984).

63. A. Attar, Coal Proc. Tech., 4, 26(1978).

64. ASTM, Part 26D2492, 507(1974).

65. British Standard Institution, BS1016, Part II (1985).

66. International Organization for Standardization, R156 (1960).

67. A. W. Deubrouck, "Sulfur Reduction Potential of the Goals of the United States," U. S. Bureau of Mines, RI7633, Washington, D. C. (1972).

68. W. H. Ode, "Coal Analysis and Mineral Matter" in "Chemistry of Coal Utilization," Supplementary Vol., H. H. Lowry (ed.), Wiley, New York, p.215, (1963).

69. H. J. Gluskoter and J. A. Simon, Illinios State Geo. Survey, Circular 432, (1968).

70. D. A. D. Boateny and C. R. Phillips, Fuel, 55, 318(1976).

71. H. J. Gluskoter, ASC Div. Fuel Chem., 20(2), 94(1975).

72. R. D. Snow, J. Prakt. Chem., 122, 1(1929).

73. A. Attar, W. H. Corcoran and G. Gibson, ACS Div. Fuel Chem., 21(7), 106(1976).

74. S. Caroli, A. Mazzeo, A. Laurenzi, O. Senofonte and N. Violante, J. Anal. At. Spectrosc., 3, 245(1988).

75. "Annual Book of ASTM Methods," Method D4239, Philadelpnia (1985).

APPENDEX

IONIZATION TEMPERATURE PROGRAM

```
10  PRINT "THIS PROGRAM BY J. BOLTON AND L. PERKINS"
20  PRINT "WILL TAKE EXPERIMENTAL ION/ATOM RATIOS"
30  PRINT "AND CALCULATE A CORRESPONDING T(ION)"
40  PRINT "       1     CA          4     CD"
50  PRINT "       2     BA          5     ZN"
60  PRINT "       3     MG          6     SR"
70  GET G$: IF G$ = "" THEN 70
80  IF G$ = "1" THEN 630
90  IF G$ = "2" THEN 640
100  IF G$ = "3" THEN 650
110  IF G$ = "4" THEN 660
120  IF G$ = "5" THEN 670
130  IF G$ = "6" THEN 680
140  INPUT "ENTER EXCITATION TEMPERATURE";T
145 S = T
150  INPUT "ION/ATOM RATIO";I
160  INPUT "ELECTRON DENSITY";N
170 Y = G(1) * G(2)
180 J = (V(1) - V(2) + V(3))
190 K = J / T
200 M =  - 11600 * K
210 L =  EXP (M)
220 X = ((4.83E15) / (N)) * Y * (T ^ 1.5) * L
```

```
230  IF (I - X) > 20 THEN 470
240  IF (I - X) > 10 THEN 480
250  IF (I - X) > 5 THEN 490
260  IF (I - X) > 1 THEN 500
270  IF (I - X) > .1 THEN 510
280  IF (I - X) <  - 20 THEN 550
290  IF (I - X) <  - 10 THEN 560
300  IF (I - X) <  - 5 THEN 570
310  IF (I - X) <  - 1 THEN 580
320  IF (I - X) <  - .1 THEN 590
330  PR# 1
340  PRINT "FROM THE DATA ENTERED"
350  PRINT "TEMPERATURE ";S
360  PRINT "ION/ATOM RATIO ";I
370  PRINT "ELECTRON NUMBER DENSITY ";N
380  PRINT "THE EXPERIMENTAL TEMPERATURE IS ";T
390  PRINT "THE EXPERIMENTAL ION TO ATOM RATIO IS    ";X
400  PR# 3
410  PRINT "DO YOU WANT TO MAKE ANOTHER RUN?"
420  GET A$: IF A$ = "" THEN 420
430  IF A$ = "N" THEN 450
440  IF A$ = "Y" THEN 10
450  PRINT "GOOD BYE"
460  END
470 Z = 20: GOTO 520
```

```
480  Z = 10: GOTO 520
490  Z = 5:  GOTO 520
500  Z = 1:  GOTO 520
510  Z = .1:  GOTO 520
520  T = T + Z
530  PR# 3
540  PRINT "T=";T,"X=";X: GOTO 170
550  Z = 20 : GOTO 600
560  Z = 10 : GOTO 600
570  Z = 5 : GOTO 600
580  Z = 1 : GOTO 600
590  Z = .1 : GOTO 600
600  T= T - Z
610  PR# 3
620  PRINT "T=";T,"X=";X: GOTO 170
630  V(1) = 6.111:V(2) = 2.936:V(3) = 3.152:G(1) =
     64.63:G(2) = 1.495E-2: GOTO 140
640  V(1) = 5.122:V(2) = 2.241:V(3) = 2.724:G(1) =
     124.4:G(2) = 1.028E-2: GOTO 140
650  V(1) = 7.644:V(2) = 4.350:V(3) = 4.43:G(1) =
     19.81:G(2) = 3.721E-2: GOTO 140
660  V(1) = 8.991:V(2) = 5.420:V(3) = 5.470:G(1) =
     14.39:G(2) = 2.649E-2: GOTO 140
670  V(1) = 9.391:V(2) = 5.800:V(3) = 6.130:G(1) =
     10.06:G(2) = 6.519E-2: GOTO 140
680  V(1) = 5.692:V(2) = 2.692:V(3) = 3.040:G(1) =
     76.40:G(2) = 1.393E-2: GOTO 140
```

ELECTRON NUMBER DENSITY PROGRAM

```
10  REM Electron Number Density by G. Long and J. Bolton,
    VPI (8/18/88)

20  REM ref H. R. Griem, Spectral Line Broadening by
    Plasmas, Academic press, NY, NY (1984) QC718.5 S6 G74

30  PR# 3

40  HOME

50  PRINT: PRINT "Electron Number Density"

60  PRINT: PRINT "This program will calculate the electron
    number density of a"

70  PRINT "plasma based upon the Stark broadening of the H
    beta line"

80  PRINT: INPUT "Enter the monochromator scan speed
    (A/s).":M

90  PRINT: INPUT "Enter the chart recorder speed
    (cm/min).":CR

100 PRINT: INPUT "IS the plasma temperature below 5000K
    (Y/N)";PT$

110 PRINT: INPUT "Do you want a printed copy (Y/N)";PD$

120 IF PT$ = "Y" THEN 140

130 C = 3.68E14: GOTO 140

140 C = 3.84E14

150 HOME: INPUT "Enter the title of the data";D$

160 PRINT: INPUT "Enter the 1/2 width in cm.";CM

170 REM CALC OF HW

180 HW = (M * 60 * CM) / CR

190 REM SCREEN DUMP

200 HOME: GOSUB 310
```

```
210  REM PRINTER DUMP
220  IF PD$ = "N" THEN 280
230  PR#1
240  GOSUB 310
250  PRINT: PRINT
260  PR# 0
270  PR# 3
280  VTAB (20): INPUT"Another run with the same scan speeds
     (Y/N)";AN$
290  IF AN$ = "Y" THEN 150
300  GOTO 400
310  REM CALC SUBRTN
320  HW = (M * 60 * CM) / CR
330  PRINT: PRINT D$
340  PRINT: PRINT " Half width is "HW" A"
350  REM CALC OF Ne-
360  NE = C * ((HW) ^ 1.5)
370  N = (INT (NE / 1E13)) * 1E13
380  PRINT: PRINT "Number density is "N" e-/cc."
390  RETURN
400  HOME: VTAB (13): HTAB (35): FLASH: PRINT"Goodbye":
     NORMAL: VTAB (20): END
```

The three page vita has been removed from the scanned document. Page 1 of 3

The three page vita has been removed from the scanned document. Page 2 of 3

The three page vita has been removed from the scanned document. Page 3 of 3